Monthly Notices of the ROYAL ASTRONOMICAL SOCIETY

MNRAS **504,** 4667–4686 (2021) doi:10.1093/mnras/stab1150
Advance Access publication 2021 April 23

The completed SDSS-IV extended Baryon Oscillation Spectroscopic Survey: N-body mock challenge for the eBOSS emission line galaxy sample

Shadab Alam,[1★] Arnaud de Mattia,[2] Amélie Tamone,[3] S. Ávila,[4,5] John A. Peacock,[1] V. Gonzalez-Perez,[6,7] Alex Smith,[8] Anand Raichoor,[3] Ashley J. Ross,[9] Julian E. Bautista,[10] Etienne Burtin,[2] Johan Comparat,[11] Kyle S. Dawson,[12] Hélion du Mas des Bourboux,[12] Stéphanie Escoffier,[13] Héctor Gil-Marín,[14,15] Salman Habib,[16,17] Katrin Heitmann,[16] Jiamin Hou,[18] Faizan G. Mohammad,[19,20] Eva-Maria Mueller,[21] Richard Neveux,[2] Romain Paviot,[13,22] Will J. Percival,[19,20,23] Graziano Rossi,[24] Vanina Ruhlmann-Kleider,[2] Rita Tojeiro,[25] Mariana Vargas Magaña,[26] Cheng Zhao[3] and Gong-Bo Zhao[10,27,28]

Affiliations are listed at the end of the paper

Accepted 2021 April 12. Received 2021 March 13; in original form 2020 July 17

ABSTRACT

Cosmological growth can be measured in the redshift space clustering of galaxies targeted by spectroscopic surveys. Accurate prediction of clustering of galaxies will require understanding galaxy physics, which is a very hard and highly non-linear problem. Approximate models of redshift space distortion (RSD) take a perturbative approach to solve the evolution of dark matter and galaxies in the universe. In this paper, we focus on extended Baryon Oscillation Spectroscopic (eBOSS) emission line galaxies (ELGs) that live in intermediate mass haloes. We create a series of mock catalogues using haloes from the Multidark and OUTER RIM dark matter only N-body simulations. Our mock catalogues include various effects inspired by baryonic physics such as assembly bias and the characteristics of satellite galaxies kinematics, dynamics, and statistics deviating from dark matter particles. We analyse these mocks using the TNS RSD model in Fourier space and the convolution Lagrangian perturbation theory (CLPT) in configuration space. We conclude that these two RSD models provide an unbiased measurement of RSD within the statistical error of our mocks. We obtain the conservative theoretical systematic uncertainty of 3.3 per cent, 1.8 per cent, and 1.5 per cent in $f\sigma_8$, $\alpha_{\shortparallel}$, and $\alpha_{\perp}$, respectively, for the TNS and CLPT models. We note that the estimated theoretical systematic error is an order of magnitude smaller than the statistical error of the eBOSS ELG sample and hence are negligible for the purpose of the current eBOSS ELG analysis.

Key words: galaxies: haloes – large-scale structure of Universe – cosmological parameters.

1 INTRODUCTION

One fundamental consideration in all astronomical studies has remained the same since the begining of astronomy. That is, the brighter galaxies are more easily detected, up to larger distances, than fainter ones. In the era of large spectroscopic follow-up (Percival et al. 2004; Schlegel, White & Eisenstein 2009; Blake et al. 2011; Beutler et al. 2012; de la Torre et al. 2013; Liske et al. 2015; Dawson et al. 2016), another important metric one has to consider is the ability to measure the redshift of galaxies. In general, this is a function of the line-flux/features in the galaxy spectral energy distribution widely known as galaxy spectrum.

One of the galaxy population known as emission line galaxies (ELGs) can be active galactic nuclei (AGNs) or star-forming galaxies. Cosmological surveys are targeting star-forming ELGs for massive spectroscopic surveys (Comparat et al. 2013a) at $z \approx 0.5-2$, as

(i) there are plenty of ELGs at that epoch when the universe had a higher star formation density;

(ii) they can provide a spectroscopic redshift measurement with a short exposure time because of strong emission lines, without needing to detect the continuum; and

(iii) there emission line can be detected using optical and near-infrared detectors.

This has led to the popularity of star-forming ELGs among the architects of galaxy redshift surveys. Hereafter, we will use ELGs to refer to star-forming galaxies with strong emission lines. Such characteristics of ELGs has led to focused ELG program in extended Baryon Oscillation Spectroscopic (eBOSS) survey (Dawson et al. 2016) and also one of the main target sample for ongoing DESI survey (DESI Collaboration 2016) that aims to allocate more than 50 per cent of its fibre budget to ELGs, leading to most precise distance constraint. Other surveys that have or will be targeting ELGs include *Euclid* (Laureijs et al. 2011), PFS (Takada et al. 2014a), WiggleZ (Blake et al. 2011), *WFIRST* (Spergel et al. 2015), and 4MOST (de Jong et al. 2014).

★ E-mail: shadab.zamman@gmail.com

Targeting special kind of galaxies means interpreting the cosmological information may become harder due to possibility of complex galaxy formation physics leaking into cosmological measurements. Star-forming galaxies typically appear blue and generally avoid very high densities (e.g Chen et al. 2017; Kraljic et al. 2018). ELGs are expected to be predominantly lower mass galaxies compared to luminous red galaxies (LRGs) avoiding the centre of massive haloes (e.g. Favole et al. 2016; Gonzalez-Perez et al. 2018; Guo et al. 2018). The complex interplay between the cosmic web and galaxy formation processes makes it more difficult to predict the dark matter haloes that hosts such galaxies. eBOSS and DESI aim to target a specific sub-sample of ELGs with high emission in [O II] 3726–3729 Å line flux. Models of galaxy formation show that formation efficiency and dynamics of such galaxy samples are sensitive to the cosmic web beyond the local density and halo mass (e.g. Gonzalez-Perez et al. 2020; Kraljic et al. 2020). Therefore, this sample will have great potential to advance our understanding of galaxy formation physics.

One of the key measurement regarding such galaxy population is the mean host halo mass or linear galaxy bias, which quantify the amplitude of the galaxy clustering compared to the dark matter. Comparat et al. (2013b) studied various photometric selection of ELG samples and measured a galaxy bias being greater than 1.5 using angular clustering and weak lensing. Mostek et al. (2013) measured galaxy bias to be 1.3–2.1 of star-forming galaxies around redshift 1 and strongly correlated with the star formation rate using the DEEP2 survey (Newman et al. 2013).

The measured redshift of galaxy consists of two components, one is the shift due to expansion of the Universe called cosmological redshift and another is the Doppler shift due to relative velocities projected along the line of sight. But in individual galaxy spectrum it is impossible to separate the two. In principle, the redshift can also be sensitive to various relativistic effects including gravitational redshift (Cappi 1995). But such effects are very small and negligible for the purpose of this study (Zhu et al. 2017; Alam et al. 2017a). The redshift space clustering of galaxies is not isotropic as distance to the galaxy inferred from their redshift are correlated with their line-of-sight velocity. This produces a distortion in the galaxy correlation function/power spectrum along line of sight compared to the plane of sky. This is known as redshift space distortions (RSDs; Peebles 1980; Kaiser 1987). The distortion pattern is a measure of galaxy peculiar velocities and hence provides measurement of growth rate at the epoch of the sample called f. On very large scales (above $\approx 50\,h^{-1}$ Mpc) the clustering of galaxies and their peculiar velocities behave linearly and therefore can be modelled with linear perturbation theory (Kaiser 1987; Hamilton 1992). But most precise measurement of galaxy clustering are obtained at quasi-linear ($\approx 35\,h^{-1}$ Mpc) and non-linear ($\approx 10\,h^{-1}$ Mpc) scales (Reid et al. 2014). Therefore, it is crucial to be able to model the redshift space clustering measurement at these quasi-linear scales. There have been several recent theoretical developement to extend the linear perturbation theory by performing various expansions and higher order calculations (e.g. Matsubara 2008b; Taruya, Nishimichi & Saito 2010; Carlson, Reid & White 2013; Okumura et al. 2014; Vlah, Castorina & White 2016).

One of the primary cosmological goals of galaxy redshift surveys is to measure the angular diameter distance [$D_M(z)$], the Hubble constant [$D_H(z) = c/H(z)$], and the growth rate of structure [$f\sigma_8(z)$] through RSD, where σ_8 is the amplitude of the matter fluctuation at $8\,h^{-1}$ Mpc scale. Such measurements when combined with results from the cosmic microwave background (Bennett et al. 2013; Planck Collaboration VI 2018) provide the strongest constraints on the ingredients of the Universe such as the amount of dark matter and the geometry of the Universe (Alam et al. 2017b). This also provides some of the strongest constraints on models of modified gravity, in particular for those driven by measurements of the growth rate ($f\sigma_8$; e.g. Alam, Ho & Silvestri 2016; Mueller et al. 2018).

Table 1. The eBOSS final cosmological interpretation is presented in Alam et al. (2020) and galaxy catalogues are described in Raichoor et al. (2020), Ross et al. (2020), and Lyke et al. (2020). Mock catalogues used for covariance matrix and systematic studies is described in Zhao et al. (2021) and Lin et al. (2020). A summary of all SDSS BAO and RSD measurements with accompanying legacy figures can be found here. The full cosmological interpretation of these measurements can be found here. Analysis for each of the tracers are presented in papers given below.

Tracers	$\xi_\ell(s)$	$P_\ell(k)$	Mock challenge
ELG	Tamone et al. (2020)	de-Mattia et al. (2020)	This work
LRG	Bautista et al. (2020)	Gil-Marin et al. (2020)	Rossi et al. (2020)
QSO	Hou et al. (2020)	Neveux et al. (2020)	Smith et al. (2020)
Ly α	du Mas des Bourboux et al. (2020)		

In this paper, we focus on two models of RSD namely TNS (Taruya et al. 2010) for the power spectrum and convolution Lagrangian perturbation theory (CLPT)–Gaussian Streaming Redshift Space Distortions (GSRSD) (Wang, Reid & White 2014) for the correlation function. Ideally, one needs to test the RSD models with mock catalogues produced by solving full physics of galaxy formation along with dark matter dynamics. But currently the best simulation of structure formation known as hyro-dynamical simulations involve various approximation and do not completely reproduce the observed galaxy colour and clustering (see figs 8 and 16 in Renneby et al. 2020). Such hydro-dynamical simulations are also computationally expensive and can only be produced in small volume (Schaye et al. 2010, 2015; Dubois et al. 2014; McCarthy et al. 2017; Pillepich et al. 2018; Davé et al. 2019). Therefore, we adapt halo occupation distribution (HOD) models (Benson et al. 2000; Peacock & Smith 2000; Seljak 2000; White, Hernquist & Springel 2001; Berlind & Weinberg 2002; Cooray & Sheth 2002) for ELG using N-body simulations to produce mock galaxy catalogues occupying large volumes (e.g. Alam et al. 2019). We first test the RSD models through a series of non-blind mocks with a variety of baryonic physics added to the mock catalogues. The analysis choices such as priors, range of scales etc., were fixed based on tests on these non-blind mocks. The non-blind mocks means all the true cosmological parameters of the mocks is known to the group analysing them. We then follow our tests with a set of blind mock in order to avoid any confirmation bias present in the initial non-blind analysis. The blind mocks use known underlying cosmology but has an unkown value for the growth rate that is revealed only after the analysis is finished. This allowed us to asses the presence of any systematic biases in the measurements, arising from limitations in the theoretical RSD models.

This study is part of a series of papers analysing the complete eBOSS sample from data release 16 (DR16). Table 1 provide a full list of the papers involved in obtaining cosmological constraint from eBOSS DR16. This paper is organized as follows. We first describe the eBOSS ELG sample in Section 2. The models of RSDs are described in Section 3. The N-body simulations used in this paper are described in Section 4. The details on method to obtain summary statistics from galaxy catalogues is given in Section 5. The models for ELGs are described in Section 6. The details on unblinded tests of RSD model given in Section 7 and blinded tests are discussed in Section 8. We finally provide the systematic errors in the RSD models in Section 9 and conclude in Section 10.

2 EBOSS ELG DATA

The eBOSS (Dawson et al. 2013) project is one of the programmes within the wider 5-yr Sloan Digital Sky Survey-IV (SDSS-IV; Blanton et al. 2017) using BOSS spectrograph (Smee et al. 2013) on the 2.5-m Sloan Telescope (Gunn et al. 2006). The eBOSS sample consists of four different types of tracers, namely LRGs (Prakash et al. 2016), ELG (Raichoor et al. 2017), quasi-stellar objects (QSO; Myers et al. 2015) used as direct tracers of the matter field, and QSOs at higher redshifts ($z > 2.2$), for studies of the Ly α forest (Palanque-Delabrouille et al. 2016). In this paper we are focusing on testing theoretical models for ELGs, a similar tests have been presented in Smith et al. (2020) for QSO and Rossi et al. (in preparation) for LRGs.

The eBOSS ELGs are selected based on high [O II] flux and are expected to be mostly star-forming galaxies typical of the population at high redshift. An earlier study about ELG selection with the SDSS infrastructure was performed by Comparat et al. (2013a,b) and a pilot survey of ELG testing different target selection algorithms is reported in Comparat et al. (2016). The ELG sample in eBOSS is selected from intermediate release (DR3/DR5; Raichoor et al. 2016) of the *grz*-photometry of the Dark Energy Camera Legacy survey (Dey et al. 2019). The target selection rules for ELGs in the North Galactic Cap (NGC) and South Galactic Cap (SGC) are slightly different due to the availability of deeper data in the SGC. The ELG selection has two parts, the first of which is to select star-forming galaxies corresponding to the [O II] emission and the second is to preferentially select galaxies around in $0.6 < z < 1.1$ (Comparat et al. 2015). More details of how these rules were derived and additional considerations are discussed in Raichoor et al. (2017). The final sample consists of 173 736 number of ELG galaxies covering a combined area of 730 deg^2, after veto mask applied, in two different fields (NGC, SGC). The final large-scale structure catalogue including systematic weights and observational efficiency is described in Raichoor et al. (2020).

3 REDSHIFT SPACE DISTORTIONS MODELS

In this paper, we focus on two models of RSDs namely TNS (Taruya et al. 2010) for the power spectrum and CLPT–GSRSD (Wang et al. 2014) for the correlation function. We briefly summarize the main ingredients of these models below.

3.1 TNS model

One of the successful analytical model for the redshift space galaxy power spectrum was proposed by Taruya et al. (2010) and known as TNS model. The redshift-space power spectrum in the TNS model is given by

$$P_{\rm g}(k,\mu) = P_{\rm TNS}(k) D_{\rm FOG}(k,\mu,\sigma_{\rm v}), \tag{1}$$

where k is the magnitude of the wavenumber, $\sigma_{\rm v}$ representing the velocity dispersion of satellite galaxies, and μ represents the cosine of the angle from the line of sight. The $D_{\rm FoG}$ is the Finger-of-God (FoG) terms that leads to the suppression of the power spectrum due to the randomness of galaxy peculiar velocities at small scales associated with satellite galaxies. We are using a Lorentzian form $D_{\rm FoG}(k,\mu,\sigma_{\rm v}) = (1 + 0.5(k\mu\sigma_{\rm v})^2)^{-2}$. The TNS model non-linear power spectrum $P_{\rm TNS}(k)$ is given by

$$P_{\rm TNS}(k) = P^g_{\delta\delta}(k) + 2f\mu^2 P^g_{\delta\theta}(k) + f^2\mu^4 P_{\theta\theta}(k) + C_b(b_1), \tag{2}$$

where f is the growth rate and b_1 is the linear galaxy bias. The galaxy–galaxy [$P^g_{\delta\delta}(k)$], galaxy–velocity [$P^g_{\delta\theta}(k)$], velocity–velocity [$P_{\theta\theta}(k)$] power spectra and the RSD correction term C_b are calculated using RegPT (Taruya et al. 2010) scheme at 2-loop order. Note that the bias terms involved in $P^g_{\delta\delta}$, $P^g_{\delta\theta}(k)$, and $P_{\theta\theta}(k)$ are calculated following McDonald & Roy (2009) and Beutler et al. (2017). The linear matter power spectrum, which is the input to the perturbative calculation, is computed at the fiducial cosmology using the Boltzmann code `CLASS` (Blas, Lesgourgues & Tram 2011).

The robustness and precision of this theoretical model is tested in this paper using accurate N-body based mocks with diverse galaxy physics models. This model is used to measure the RSD signal in the eBOSS ELG power spectrum de-Mattia et al. (2020). We suggest de-Mattia et al. (2020) for further details about the implementation of this model.

3.2 CLPT–GSRSD model

The RSD is essentially the effect caused by the convolution of the line-of-sight component of the velocity field with the spatial distribution of galaxies, i.e. the galaxy clustering (Reid & White 2011). Therefore, a simple approach to model the redshift space correlation function of galaxies is by proposing a model for this convolution along with a model to predict the galaxy clustering and velocity field. In this model, we used a Gaussian Streaming (Reid & White 2011; Wang et al. 2014) model for the convolution and the CLPT (Carlson et al. 2013) to predict the inherent galaxy clustering and velocity field.

The redshift space correlation function ($\xi(s_{\shortparallel}, s_{\perp})$) as the function of redshift space separations, along line of sight ($s_{\shortparallel}$) and perpendicular to the line of sight ($s_{\perp}$), in the Gaussian streaming model (GSRSD) can be written as follows:

$$1 + \xi(s_{\parallel}, s_{\perp}) = \int (1 + \xi(r)) \mathcal{G}(s_{\parallel} - r_{\parallel}, v_{12}, \sigma_{12}) {\rm d}^3 r, \tag{3}$$

where $\xi(r)$, $v_{12}(r)$, and $\sigma_{12(r)}$ are the real space correlation function, the pairwise infall velocity, and the pairwise velocity dispersion as the function of real space separation (r) between a pair of galaxies. $\mathcal{G}$ describes the probability that a pair of galaxies with separation along the line of sight ($r_{\shortparallel}$) in real space have a separation ($s_{\shortparallel}$) in redshift space. $\mathcal{G}$ is given by following equation:

$$\mathcal{G}(s_{\parallel} - r_{\parallel}, v_{12}, \sigma_{12}) = \frac{1}{\sqrt{2\pi\sigma^2_{12}(r,\mu)}} \exp\left(\frac{(s_{\parallel} - r_{\parallel} - \mu v_{12})^2}{2\sigma^2_{12}(r,\mu)}\right), \tag{4}$$

where the real space statistics [$\xi(r)$, $v_{12}(r)$, $\sigma_{12(r)}$] are calculated using the CLPT, which is based on the Lagrangian perturbation theory (LPT; Matsubara 2008a; Matsubara 2008c). LPT focuses on solving equation of motion of the universe for the displacement field perturbatively as follows:

$$\vec{\psi}(\vec{q},t) = \vec{x}(\vec{q},t) - \vec{q} \approx \vec{\psi}^{(1)} + \vec{\psi}^{(2)} + \vec{\psi}^{(3)} + \vec{\psi}^{(4)} \cdots, \tag{5}$$

where $\vec{x}(\vec{q},t)$ and $\vec{q}$ are the final and initial positions of the particles at time t. The displacement field, $\vec{\psi}(\vec{q},t)$, is expanded as a series of perturbations ψ^i, where the first order term is the Zel'dovich approximation. The CLPT model identifies terms in the expansion of the density field correlator $<\delta_1\delta_2>$, which become constant in the limit of large scales and kept from being expanded. This essentially leads to a resummation of LPT with additional terms being exact, leading to a more accurate predictions. Finally, this model takes the linear matter power spectrum, galaxy bias, growth rate, and predicts the non-linear redshift space correlation function multipoles (see

Section 5 for details), which are used to perform the measurements of mocks N-body galaxy mock catalogue in this paper.

4 SIMULATIONS

In this paper, we use dark matter halo catalogues from two different N-body simulations. Mock catalogues are constructed from the simulation snapshot at $z = 0.86$, as it is closest in redshift to the effective redshift of the eBOSS ELG sample ($z_{\rm eff} = 0.85$). We briefly describe these simulations in the following subsections.

4.1 MultiDark Planck 2

The MultiDark Planck 2 (MDPL2; Klypin et al. 2016) simulation is publicly available through the CosmoSim data base[1] (Prada et al. 2012; Riebe et al. 2013). MDPL2 is a N-body simulation run, consists of gravity-only, generated using the GADGET-2 code. The simulation assumes a flat ΛCDM cosmology with $\Omega_m = 0.307$, $\Omega_b = 0.048$, $h = 0.67$, $n_s = 0.96$, and $\sigma_8 = 0.82$. This simulation uses 3840^3 particles with mass of $1.51 \times 10^9\, h^{-1}\, {\rm M}_\odot$ in a periodic box of side length $1000\, h^{-1}$ Mpc. A halo catalogue using the ROCKSTAR[2] phase space halo finder (Behroozi, Wechsler & Wu 2013) at an effective redshift of $z \approx 0.86$ snapshot was constructed. ROCKSTAR starts with a Friends-of-Friends (FoF) group catalogue and analyses particles in full phase space (i.e. position and velocity) in order to define halo properties and robustly identify the substructures. From the halo catalogue of the simulation, we only use the main haloes, removing all the subhaloes and modelling satellite galaxies as described in Section 6.

4.2 OUTER RIM

The OUTER RIM N-body simulation (OR; Habib et al. 2016; Heitmann et al. 2019) is one of the largest high resolution N-body simulation. OUTER RIM consists of gravity-only and runs using Hardware/Hybrid Accelerated Cosmology Code. This simulation uses a flat ΛCDM WMAP7 (Komatsu et al. 2011) cosmology with $\Omega_{\rm cdm}h^2 = 0.1109$, $\Omega_{\rm b}h^2 = 0.02258$, $h = 0.71$, $\sigma_8 = 0.8$, and $n_s = 0.963$. This simulation uses $10\,240^3$ particles of mass $m_{\rm p} = 1.85 \times 10^9\ h^{-1}\, {\rm M}_\odot$ in a periodic box of side length $3\ h^{-1}$ Gpc. A halo catalogue using the FoF algorithm (Davis et al. 1985) with linking length $b = 0.168$ at an effective redshift of $z = 0.865$ snapshot was constructed.

5 MEASUREMENTS

For each of the mock galaxy catalogue, we measure the power spectrum and the correlation function multipoles along with the corresponding covariance matrices. These multipoles are then fitted with the corresponding RSD models in order to perform a measurement of the growth rate along with the geometry of the Universe.

The first step requires obtaining galaxy catalogues with their respective redshift space positions. A given mock galaxy catalogue consists of a list of galaxy positions and velocities in a 3D cubic box with periodic boundary conditions. We first choose one of the axis as line of sight. This is then used to determine the redshift space positions of galaxies as follows:

$$\vec{s} = \vec{r} + \hat{los} \cdot \vec{v}/aH, \tag{6}$$

where $\vec{s}$, $\vec{r}$, and $\vec{v}$ are the redshift space position, real space position, and galaxy velocities in unit of distance. The $\hat{los}$ is the vector pointing to line-of-sight direction, for example, if the z-axis is chosen to be the line of sight, then $\hat{los} = 0\hat{x} + 0\hat{y} + 1\hat{z}$. Note that the redshift space transformation is performed with periodic boundary conditions. Below, we describe the details of this measurement process starting from the galaxy catalogue in redshift space ($\vec{s}$).

5.1 Measurement in Fourier space [$P_\ell(k)$]

We first take the redshift space galaxy catalogue and estimate the density contrast ($\delta_g(\vec{s})$) on a regular grid of mesh size 512^3 using the triangular shaped cloud scheme. The Fourier transformation of the density contrast $\delta_g(\vec{k})$ is then used to estimate the power spectrum as follows:

$$P_\ell(k) = (2\ell + 1) \int \frac{{\rm d}\Omega_k}{4\pi\, V} \delta_g(\vec{k}) \delta_g^*(\vec{k}) \mathcal{L}_\ell(\hat{\vec{k}} \cdot \hat{los}) - P_\ell^{\rm noise}(k)\,. \tag{7}$$

$\mathcal{L}_\ell$ is the Legendre polynomial of order ℓ and $\hat{los}$ the chosen line-of-sight vector. $P_\ell^{\rm noise}(k)$ is the shot noise term, which is given by the inverse of mean number density for the monopole ($\ell = 0$) and is zero otherwise. The `nbodykit` (Hand et al. 2018) package is used to perform the calculation of the power spectrum. The use of a regular grid to perform the fast Fourier transformation makes the angular modes distribution irregular at large scales. This affect the final measured power spectrum that we account for in the model by weighting the modes according to the $(k, \hat{\vec{k}} \cdot \hat{los})$ sampling.

We finally fit the TNS model for redshift space power spectrum (see Section 3.1) to the measured power spectrum multipoles from N-body simulations. The fit involves three cosmological parameters, which are the growth rate $f = \frac{{\rm d}\ln D(a)}{{\rm d}\ln a}$ and two scaling parameters $\alpha_\perp = \frac{D_M(z) r_s^{\rm fid}}{D_M^{\rm fid}(z) r_s}$ and $\alpha_\parallel = \frac{H^{\rm fid}(z) r_s^{\rm fid}}{H(z) r_s}$.

$$\alpha_\perp = \frac{D_M(z) r_{\rm s}^{\rm fid}}{D_M^{\rm fid}(z) r_{\rm s}}, \tag{8}$$

$$\alpha_\parallel = \frac{H^{\rm fid}(z) r_{\rm s}^{\rm fid}}{H(z) r_{\rm s}}, \tag{9}$$

where $r_{\rm s}$ is the comoving sound horizon scale. The Alcock–Paczynski (AP) parameters ($\alpha_\perp$, $\alpha_{\shortparallel}$) compress cosmological information efficiently by rescaling the distances over the line of sight and perpendicularly to it. Given that the growth rate is degenerate with the normalization of the power spectrum σ_8, we always quote measurement of $f\sigma_8$ rather than f itself. Apart from these we also have four nuisance parameters, the two bias parameters b_1, b_2, one velocity dispersion to account for non-linear FoGs σ_v and the stochastic shot noise term A_g. The fitted k-range of the RSD measurement is 0.02–0.2 Mpc$^{-1}\, h$ for the monopole and quadrupole and 0.02–0.15 Mpc$^{-1}\, h$ for the hexadecapole (see de-Mattia et al. (2020) for details). We perform a χ^2 minimization using the `Minuit` (James & Roos 1975)[3] package, with wide priors for all parameters. We perform several tests, including a test on the parameter boundaries to make sure the results are robust. Errors on the parameters are given by likelihood profiling at the $\Delta\chi^2 = 1$ level.

MultiDark mocks are analysed within the fiducial cosmology of eBOSS analyses (de-Mattia et al. 2020) and thus treated as non-periodic; the induced window function effect and global integral constraint are accounted for in the model, following Wilson et al. (2017), and de Mattia & Ruhlmann-Kleider (2019), respectively. The

[1] https://www.cosmosim.org/cms/simulations/mdpl2/
[2] https://bitbucket.org/gfcstanford/rockstar
[3] https://github.com/iminuit/iminuit

covariance matrix is estimated from 500 lognormal mocks generated with the MultiDark cosmology, with a bias of 1.4, and the same density as MultiDark mocks: $3 \times 10^{-3}\ h^3\,\mathrm{Mpc}^{-3}$. For the OUTER RIM mocks, we use a Gaussian covariance matrix for the measured power spectrum following the method described in Grieb et al. (2016), which has been shown to be accurate enough in the quasi-linear regime probed by RSD analyses.

5.2 Measurement in configuration space [$\xi_\ell(s)$]

For the measurement of the galaxy two-point correlation function, we first perform a pair count of galaxies (called *DD*) in redshift-space as the function of the distance between a pair of galaxies (s) and the cosine of the angle of the separation vector from the line-of-sight direction (μ). We then estimate analytically, the pair count (called *RR*) for points that are uniformly randomly distributed inside the simulation box with the same density as galaxies, using the following equation:

$$RR(s,\mu) = \frac{N_{\rm gal}(N_{\rm gal}-1)}{L_{\rm box}^3}\left[\frac{4\pi(s_2^3-s_1^3)}{3}\right][\mu_2-\mu_1]\,, \tag{10}$$

where $N_{\rm gal}$ and $L_{\rm box}$ are the number of galaxies and the size of the simulation box, respectively. s_1 and s_2 correspond to the lower and upper limits of the radial bins, while $\mu_1 = \cos(\theta_1)$ and $\mu_2 = \cos(\theta_2)$ correspond to the lower and upper limits of the angular bins. We finally obtain the correlation function multipole as follows:

$$\xi_{2D}(s,\mu) = \frac{DD(s,\mu)}{RR(s,\mu)} - 1\,, \tag{11}$$

$$\xi_\ell(s) = \frac{2\ell+1}{2}\int_\mu \xi_{2D}(s,\mu)\mathcal{L}_\ell(\mu)\mathrm{d}\mu\,, \tag{12}$$

where $\mathcal{L}_\ell$ is the Legendre polynomial of order ℓ. The periodic boundary condition allows the use of an analytic RR pair-count that makes the computation of the correlation function very efficient.

Similar to the power spectrum analysis, we use a Gaussian covariance matrix for the measured correlation function following the method described in Grieb et al. (2016).

We finally fit the CLPT model for the redshift space correlation function (see Section 3.2) to the measured correlation function multipoles from N-body simulations. The fit involves three cosmological parameters, which are the growth rate, f, and the two scaling parameters, $\alpha_\perp$ and $\alpha_\parallel$. Similar to the power spectrum analysis, we always quote measurements of $f\sigma_8$ rather than f itself. Apart from these we also have three nuisance parameters, the two Lagrangian bias parameters F_1 and F_2, and one velocity dispersion to account for non-linear FoGs $\sigma_{\rm FoG}$. Only the first-order Lagrangian bias (F_1) is allowed to be free and the second-order Lagrangian bias (F_2) is determined via the peak-background split relation (White 2014). The fitted s-range of the RSD measurement is 32–160 h^{-1} Mpc for the monopole , the quadrupole and the hexadecapole. We perform a χ^2 minimization using the `Minuit` package, with wide priors for all parameters. We perform several tests similar to the power spectrum analysis to make sure the results are robust. Errors on the parameters are given by likelihood profiling at the $\Delta\chi^2 = 1$ level.

6 EMISSION LINE GALAXIES MODELS USING HOD

Modelling large cosmological volumes of the Universe requires a certain knowledge of galaxy formation. What makes it possible for galaxies to form and what decides properties of these galaxies. The standard model within the hierarchical structure formation suggests that the dark matter collapsing under gravity throughout the evolution of the Universe forms the back bone structure and leads to the formation of the cosmic web (Mo, van den Bosch & White 2010; Wechsler & Tinker 2018). This cosmic web consists of collapsed dark matter objects called dark matter haloes that are the natural places for galaxies to form. Therefore, the two main popular models to populate large dark matter (N-body) simulations are the HOD (Benson et al. 2000; Peacock & Smith 2000; Seljak 2000; White et al. 2001; Berlind & Weinberg 2002; Cooray & Sheth 2002) and subhalo abundance matching (Kravtsov et al. 2004; Tasitsiomi et al. 2004; Vale & Ostriker 2004). These two modelling techniques assume that all galaxies are formed in dark matter haloes and that the properties of galaxies are dominantly determined by the mass of the haloes. Alternatively, one could use full hydro-dynamical simulations (Schaye et al. 2010, 2015; Dubois et al. 2014; McCarthy et al. 2017; Pillepich et al. 2018; Davé et al. 2019) or semi-analytical models (SAMs: Guo et al. 2011; Gonzalez-Perez et al. 2014). The HOD is one of the fastest and simplest way to create mock galaxy catalogues and thus is adequate for the large exploration of different mock catalogues that is done here.

In the HOD framework, we consider two kinds of galaxies in each halo known as the central and satellite galaxies. The occupation recipe provides the probability of a given halo to have a central galaxy and a number of satellite galaxies. There are various degrees of freedom in terms of how the velocities and positions of satellite galaxies are assigned within haloes and they depend on the details of the galaxy population (Reid et al. 2014; Alam et al. 2020). We aim to study a wide variety of HOD models covering a range of physical processes to estimate the robustness of our measurement independently of the details of galaxy physics. In this paper, we are using three different parametrizations of the average HOD and a variety of satellite models. Below, we describe the three parametrizations used for the shapes of the HOD for central and satellite galaxies.

6.1 Standard HOD model

The idea of hierarchical clustering brings a very simple assertion that dark matter haloes with more mass will have more baryons and hence will host more massive galaxies which will also be brighter. Therefore, we can simply rank order the dark matter haloes by their mass and galaxies by their brightness and connect them one-to-one with some dispersion. This intuitive picture about the connection between dark matter haloes and galaxies has been remarkably useful. The popular five parameter standard HOD model (hereafter SHOD) is shown to describe the mean occupation probability for the detailed hydro-dynamical models and SAMs of galaxy formation (Zheng et al. 2005; White et al. 2011).

This essentially says that the massive dark matter haloes host galaxies with constant probability and depending on the brightness limit the probability of hosting central galaxy will have a cut-off halo mass. More formally, the central occupation probability in this model is parametrized as follows:

$$p_{\rm cen}^{\rm SHOD} = \left\langle N_{\rm cen}^{\rm SHOD}(M_{\rm h})\right\rangle = \frac{1}{2}p_{\rm max}\mathrm{erfc}\left(\frac{\log_e M_{\rm c} - \log_e M_{\rm h}}{\sqrt{2}\sigma_M}\right)\,, \tag{13}$$

where $p_{\rm max}$ decides the saturation occupation probability in the high halo mass limit, and $M_{\rm c}$ and σ_M decide the cut-off halo mass and its dispersion for the given galaxy sample. Models of galaxy formation and evolution have shown that this HOD model is not adequate for star-forming galaxies in general, including star-forming ELGs (e.g. Geach et al. 2012; Contreras et al. 2013; Cochrane & Best 2018; Gonzalez-Perez et al. 2018). However, the physical processes

involved in the formation and growth of ELGs are complex and require more flexibility such as quenching at the centre of massive haloes.

6.2 High-mass quenched model

eBOSS ELGs are expected to avoid residing in the centre of massive haloes (e.g. Favole et al. 2016; Gonzalez-Perez et al. 2018; Guo et al. 2018). Such behaviour is not possible to accommodate in the SHOD model. Therefore, Alam et al. (2019) proposed a modified HOD framework encapsulating such behaviour called high-mass quenched model (HMQ). The occupation probability of central galaxy of a halo is given by the following equation:

$$p_{\rm cen}^{\rm HMQ} = \left\langle N_{\rm cen}^{\rm HMQ}(M_{\rm h})\right\rangle = 2A\phi(M_{\rm h})\Phi(\gamma M_{\rm h}) + \frac{1}{2Q}\left[1+{\rm erf}\left(\frac{\log_e M_h - \log_e M_{\rm c}}{0.01}\right)\right], \quad (14)$$

$$\phi(x) = \mathcal{N}(\log_e M_{\rm c}, \sigma_M), \quad (15)$$

$$\Phi(x) = \int_{-\infty}^{x}\phi(t){\rm d}t = \frac{1}{2}\left[1+{\rm erf}\left(\frac{x}{\sqrt{2}}\right)\right], \quad (16)$$

$$A = \frac{p_{\rm max} - 1/Q}{\max_x(2\phi(x)\Phi(\gamma x))}. \quad (17)$$

The effect of various parameters on the HMQ occupation function is illustrated in fig. 1 of Alam et al. (2019).The parameter $M_{\rm c}$ is the cut-off mass of ELG centrals impacting the location of the peak in occupation probability. Q sets the quenching efficiency for high-mass haloes; a larger value of Q implies more efficient quenching. The function $\phi(M_h)$ is the normal distribution given in equation (15) and $\Phi(M_h)$ is the cumulative density function of $\phi(M_h)$ given in equation (16). These two functions depend on the parameters γ controlling the skewness and σ_M controlling the width. The parameter A sets the overall formation efficiency of ELGs given in equation (17) and depends on $p_{\rm max}$.

6.3 Star-forming HOD

Another way to parametrize the mean HOD of ELGs is based on the results from the SAM of galaxy formation and evolution presented in Gonzalez-Perez et al. (2018), which included a simple approach to model the nebular emission in star-forming galaxies. We call this alternate parametrization (star-forming HOD, SFHOD), which was first proposed in (Avila et al. 2020) given below:

$$p_{\rm cen}^{\rm SFHOD} = \langle N_{\rm cen}^{\rm SFHOD}(M_h)\rangle = \begin{cases} \frac{A_c}{\sqrt{2\pi}\sigma}\cdot e^{-\frac{(\log_{10}M_h-\mu)^2}{2\sigma^2}} & M_h \le 10^{\mu} \\ \frac{A_c}{\sqrt{2\pi}\sigma}\cdot\left(\frac{M_h}{10^{\mu}}\right)^{\gamma} & M_h \ge 10^{\mu} \end{cases} \quad (18)$$

The parameter μ is the logarithm of the halo mass with the highest occupation probability for ELG centrals with σ giving its width and A_c overall normalization. The parameter γ suppresses the occupation probability at the high-mass ends.

The HMQ and SFHOD functional forms are closer representation of ELGs as per current understanding and expected to produce more realistic host halo distribution as observed in data. Note that the HMQ and SFHOD models will have quite different contribution to non-linearity compared to the SHOD, due to different kind of haloes hosting ELGs in the extreme ends of halo mass distribution.

6.4 Satellite galaxies

The number of satellite galaxies as a function of halo mass is given by the following functional form:

$$p_{\rm sat}\,\langle N_{\rm sat}(M_{\rm halo})\rangle = A_s\left(\frac{M_{\rm h}-\kappa M_c}{M_1}\right)^{\alpha}. \quad (19)$$

The number of satellite galaxies is assumed to be a power law with index α and characteristic satellite mass M_1. The cut-off mass is set by the parameter κ in units of $M_{\rm c}$ below which the probability of finding a satellite galaxy is zero. The parameter A_s is used to calibrate the amplitude of the satellite occupation. We use the same functional form to model the mean number of satellites for all three models (i.e. SHOD, HMQ, SFHOD), with independent parameters in each case. Satellite galaxies follow a Poisson distribution for the SHOD and HMQ models, but it has an additional free parameter β for the SFHOD model. In the SFHOD model, $\beta = 0$ is equivalent to a Poisson distribution and $0 < \beta < 1$ corresponds to a negative binomial distribution with $p = \frac{1}{1+\beta^2}$. The SFHOD model also allows satellite distribution with next integer distribution as given in equation (22) of Avila et al. (2020) and labelled as NI.

7 MOCK CHALLENGE

We create a series of mocks, from a total of 40 different models, with variations in the parameters discussed in Section 6 and beyond (Alam et al. 2019; Avila et al. 2020). As we discussed in Section 6, ELG host dark matter haloes properties are still under investigation. Therefore, the main focus here is to explore as many ways as possible to populate dark matter haloes with star-forming galaxies, to make sure the real properties of ELGs are encapsulated within the series of mocks we produce. The galaxy mocks created in this section are analysed with known expected parameters, which is a non-blind test of models. The next section describes similar tests for blind mocks.

The probability of occupying a central galaxy $\langle N_{\rm cen}\rangle$ is evaluated to create a mock galaxy catalogue for each dark matter N-body simulation box. The $\langle N_{\rm cen}\rangle$ is mainly a function of the halo mass but it may depend on other halo properties depending on the details of the model used. We then generate uniform random numbers and populate a central galaxy at the centre of the halo with the halo velocity if the random number is below $\langle N_{\rm cen}\rangle$. We then evaluate the mean number of satellite galaxies using $\langle N_{\rm sat}\rangle$ for each halo which again mainly depend on the halo mass but may depend on other halo properties. The actual number of satellites assigned to each halo is generally sampled from a Poisson distribution but for some models it follows different statistics (see Section 6). Different schemes are assumed by the models to assign the positions of satellite galaxies. They may follow an NFW distribution, a scaled NFW distribution or the distribution of randomly sampled dark matter particles from the halo. The velocities of the satellite galaxies are sampled from the velocity dispersion of haloes but some models scale the velocity dispersion by a free parameter to make the satellites hotter or cooler than dark matter particles. Some of the models also introduce an infalling velocity to the satellite. Below, we describe the details of the mock catalogues created using two sets of simulation.

7.1 MultiDark mocks

Best-fitting HOD parameters for both the SHOD and the HMQ models are obtained by fitting to the measured projected correlation function, the halo catalogue from the MultiDark simulation snapshot at redshift 0.86. The best-fitting model parameters are obtained by

Table 2. The best-fitting parameters for different HOD models and different N-body simulations. The first two columns corresponds to MultiDark and the next two for OUTER RIM. Note that the details of the SFHOD models are given in Table 4.

Parameters	MultiDark		OUTER RIM	
	SHOD	HMQ	SHOD	HMQ
$\log_{10}(M_c)$	11.70	11.6	11.4	11.5
σ_M	0.59	0.61	0.1	0.61
γ	–	4.04	–	4.04
Q	–	100	–	100
$\log_{10}(M_1)$	14.4	13.55	13.6	13.55
κ	1.0	1.0	1.0	1.0
α	0.40	0.99	0.4	0.99

minimizing the χ^2 as given below:

$$\chi^2 = \left[w_{\rm p}^{\rm eBOSS} - w_{\rm p}^{\rm model}\right]^{\rm T} \mathcal{C}^{-1} \left[w_{\rm p}^{\rm eBOSS} - w_{\rm p}^{\rm model}\right], \quad (20)$$

where $w_{\rm p}^{\rm eBOSS}$ is the measured projected correlation function from eBOSS ELG sample and $\mathcal{C}^{-1}$ is the inverse covariance matrix obtained using the jackknife resampling scheme following Alam et al. (2019). This fit was performed only for the fiducial HOD model (model = 1) and the best-fitting parameters are given in Table 2. For other variants of the HMQ and SHOD models, we keep these basic parameters fixed allowing the variation in other degrees of freedom. In principle, one could refit the basic HOD parameters along with each of the additional free parameters, but given the large errors in the HOD parameters and our focus on generating a variety with approximately the linear bias of eBOSS ELG sample, we did not performed such a refit.

The projected correlation function measured from eBOSS data and various MultiDark based mock catalogues are shown in the upper panel of Fig. 1. The black empty points show the measurement from the eBOSS sample with jackknife errors. The various coloured lines represent the projected correlation function measured from the mock catalogues. The solid lines are for HMQ models and the dashed lines are for SHOD models. The details of the different models are given in Table 3. Note that the differences in the projected clustering for different models mainly stems from the fact that we did not try to refit each model. We also show the redshift space power spectrum multipoles for each of the model in Fig. 2 with the same lines and colours convention as in the $w_{\rm p}$ plot. The monopole and quadrupole moments are shown in the top left-hand and right-hand of the plot. Bottom panels shows the ratio of monopole and qudrupole with respect to the average monopole and quadrupole of all the models.

Table 3 lists the 11 models generated for this paper. Model number 1 (i.e. HMQ1,SHOD1) is the fiducial one with halo mass only HOD and for which haloes are populated with satellites using a NFW profile for the spatial distribution along with dark matter halo velocity dispersion for redshift space positions. The next two models, 2 (i.e. HMQ2,SHOD2) and 3 (i.e. HMQ3,SHOD3), modify the concentration by populating satellite galaxies more or less concentrated by a factor of 50 per cent, respectively. The velocity dispersion for satellite galaxies is higher or lower by a factor of 50 per cent for models number 4 and 5 compared to the velocity dispersion of particles in the halo. In model number 6, we allow central galaxies to be shifted from the centre of the dark matter halo following a Gaussian distribution with width of $0.1 r_{200}$. Models number 7, 8, and 9 have assembly bias by setting the occupation of central, satellites, and both (i.e. central and satellites) to be correlated with the dark matter haloes concentration parameter. We follow the

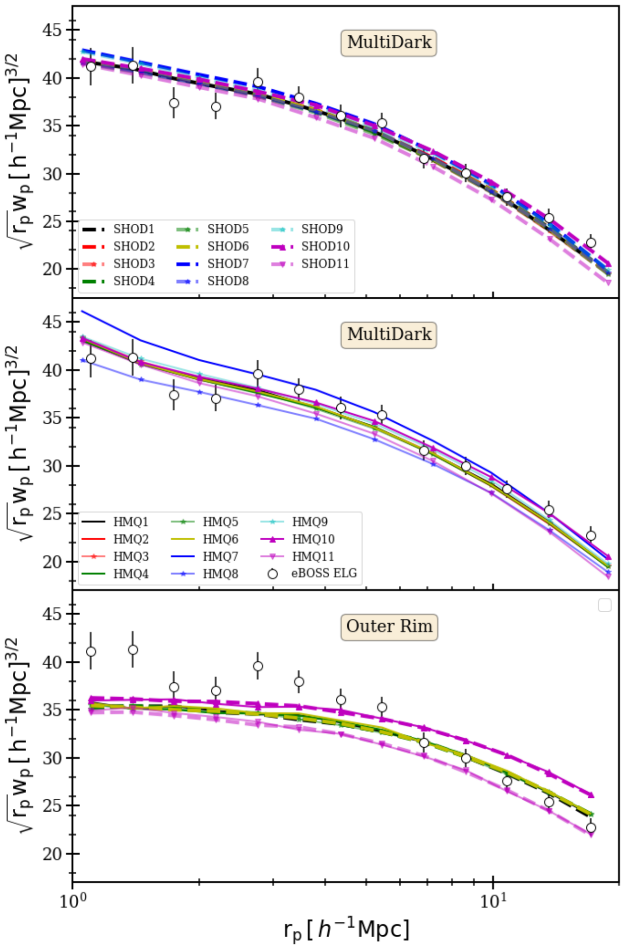

Figure 1. Project correlation function of eBOSS ELG sample along with the various non-blind mocks. The black open circles in all panels represent the w_p measured from eBOSS data. The top and middle panels show w_p for MultiDark based mocks and the bottom panel is for OUTER RIM based mocks. The solid coloured lines are for HMQ model and dashed coloured line is for SHOD models. The different colours indicating different types of models as detailed in Table 3.

scheme suggested in Zentner et al. (2019) for models with assembly bias where the occupation numbers of central and satellite galaxies are modified using the following equation:

$$\langle N_{\rm cen,sat}\rangle(M_h, c) = \langle N_{\rm cen,sat}\rangle(M_h) + (-1)^{p(c)}\delta N_{\rm cen,sat}(M_h, c), \quad (21)$$

where $\langle N_{\rm cen,\,sat}\rangle(M_h)$ is the standard occupation number of central or satellite galaxies as detailed in Section 6. The parameter c represents the dark matter halo concentration parameter. The functions $\delta N_{\rm cen}(M_h, c)$ and $\delta N_{\rm sat}(M_h, c)$ are given by following equations:

$$\delta N_{\rm cen} = A_{\rm cen}\, \mathcal{MIN}\left[\langle N_{\rm cen}\rangle(M_h), 1 - \langle N_{\rm cen}\rangle(M_h)\right] \quad (22)$$

$$\delta N_{\rm sat} = A_{\rm sat}\langle N_{\rm sat}\rangle(M_h) \quad (23)$$

where $A_{\rm cen}$ and $A_{\rm sat}$ are the two free parameters that control the level of assembly bias. The function $p(c)$ is a step function with $p(c) = 0$ for $c > = c_{\rm median}$ and $p(c) = 1$ for $c < c_{\rm median}$, where $c_{\rm median}$ is the median concentration of all the dark matter haloes. Model numbers 10 and 11 have higher or lower peculiar velocities by a factor of 20 per cent, which allows the growth rate (f) of the constructed mock catalogues to be altered keeping fixed all other parameters.

Table 3. List of SHOD and HMQ HOD models with their detailed description and simulations used. The basic HOD parameters used for these models are given in Table 2 with any additional degree of freedom described in this table.

Model	Description	Simulations
1	Fiducial HOD model: Halo mass only with dark matter distribution and kinematics for satellite galaxies	MD, OR
2	Satellite galaxies have 50 per cent higher concentration than dark matter	MD
3	Satellite galaxies have 50 per cent lower concentration than dark matter	MD
4	Satellite galaxies have 50 per cent higher velocity dispersion than dark matter	MD, OR
5	Satellite galaxies have 50 per cent lower velocity dispersion than dark matter	MD, OR
6	The central galaxies are off-centred with a Gaussian distribution of width $0.1r_{200}$	MD, OR
7	Assembly Bias: Central galaxies occupation is correlated with halo concentration ($A_{\rm cen} = 0.3$)	MD
8	Assembly Bias: Satellite galaxies occupation is correlated with halo concentration ($A_{\rm sat} = 0.3$)	MD
9	Assembly Bias: Central and Satellite galaxies occupation is correlated with halo concentration ($A_{\rm cen} = A_{\rm sat} = 0.3$)	MD
10	Peculiar velocities of galaxies are scaled higher by 20 per cent. This should increase the growth rate by 20 per cent compared to the fiducial value.	MD, OR
11	Peculiar velocities of galaxies are scaled lower by 20 per cent. This should decrease the growth rate by 20 per cent compared to the fiducial value.	MD, OR

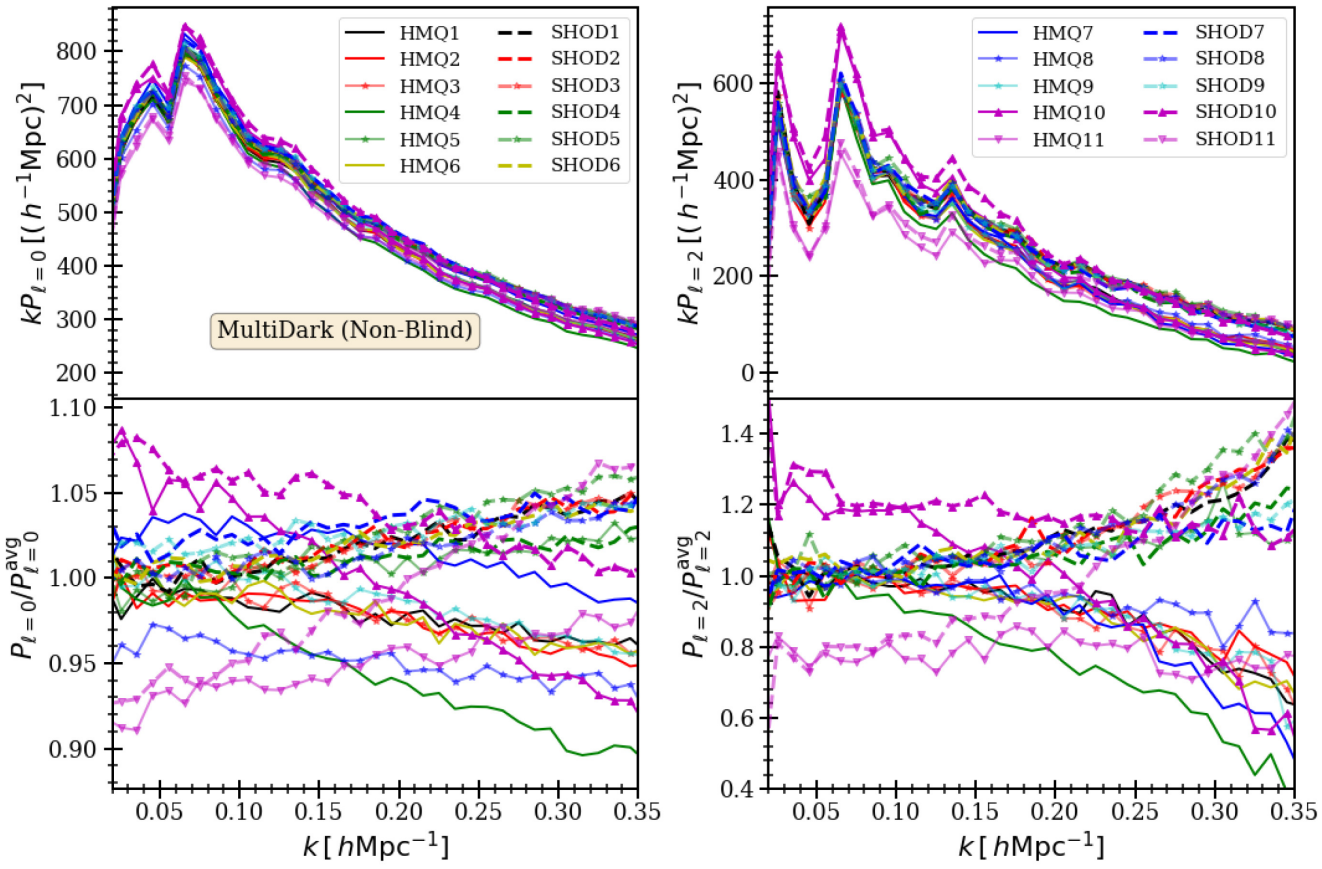

Figure 2. Power spectrum multipoles for mocks from the MultiDark simulation. The top left (right) panel shows the monopole (quadrupole) moment of the power spectrum. The bottom left (right) panel shows the ratio of monopole (quadruple) to the average power spectrum. The solid lines are for the mocks using the HMQ model and dashed are for the SHOD model. The different colours correspond to different models as described in Table 3.

Fig. 2 shows the power spectrum multipoles for the MultiDark non-blind mocks. The bottom left-hand (right-hand) panels show the monopole (quadruple) moment ratios with respect to the mean model. We notice that in the monopole the power spectrum ratio at large scales (small k) is close to 1 within 2 per cent except for models in which we scale the peculiar velocity (i.e. model numbers 10 and 11), these models show close to 10 per cent difference due to the change in the Kaiser boost factor. At small scales (large k), we see that all SHOD models (the dashed lines) have higher power in both the monopole and the quadrupole compared to HMQ models (the solid lines). The models with low or high concentration for satellite galaxies show very little difference with each other (the red coloured lines) within the range of scales studied and hence will not be causing any problem to RSD models. The green lines present models with low and high satellite velocity dispersion; these seem to affect the power spectrum significantly at these $k > 0.2\,\mathrm{Mpc}^{-1}\,h$. The models with assembly bias show differences in the power spectrum multipoles at $k > 0.2\,\mathrm{Mpc}^{-1}\,h$ and might interfere with the growth

Table 4. List of SFHOD models with their detailed description for the OUTER RIM simulation. The basic HOD parameters used for these models are set to $\mu = 11.515$, $A_c = 0.054$, $\gamma = -1.4$, $\sigma = 0.12$, $A_s = 0.053$, $\alpha = 0.9$, $\kappa = 1.0$, $M_c = 10^{\mu - 0.05}$, and $M_1 = 10^{\mu + 0.35}$. Any additional degree of freedom is described below (for further details see Avila et al. 2020).

Model	Description
1	Satellites follow a Poisson distributed, $\beta = 0$
2	Satellites follow a negative binomial distribution with $\beta = 0.1$
3	Satellites follow a negative binomial distribution with $\beta = 0.2$
4	Satellites follow the next integer from Poisson distribution, $\beta < 0$
5	Satellites have an infalling velocity following a normal distribution with mean 500 km s^{-1} and standard deviation of 200 km s^{-1}.

rate measurement if the fitting scales are pushed to such small scales. Finally, the magenta lines showing the most offset present models with scaled growth rate by 20 per cent and hence have different true cosmology and will provide a strong test of our RSD models. We note that the impact of baryonic physics on the matter power spectrum is considered to be important above $k \approx 0.3$ (van Daalen, McCarthy & Schaye 2020). But, the effect of various galaxy physics is shown at the level of 10 per cent by $k \approx 0.2$ in the quadrupole of galaxy power spectrum (see Fig. 2). Hence, the RSD analysis in this paper probes the regime affected by such beyond dark matter only physics.

7.2 OUTER RIM mocks

Using the halo catalogue from the OUTER RIM simulation snapshot at redshift 0.86 we obtain best-fitting HOD parameters for SHOD, HMQ, and SFHOD model by matching the number density and large scale galaxy bias. We do not perform a detailed model fit in this case because we are mostly interested in producing variety.

For the SHOD and HMQ models, we match the observed large scale linear bias by perturbing the best-fitting HOD parameters obtained from MultiDark mocks. The final HOD parameters used to produce the OUTER RIM mocks are given in Table 2. We produce OUTER RIM catalogues for only 6 of the 11 models as detailed in Table 3. The OUTER RIM halo catalogues do not come with a concentration parameter and therefore we do not include models that require this parameter. We do not use the concentration–mass relation as the true concentration has information about assembly of haloes that cannot be added to a concentration simply estimated from mass. Alternatively, one can fit the concentration to individual haloes in OUTER RIM but due to the size and resolution of simulation this will require significant computing power, which we consider out of the scope for this analysis. Also, we have access to only 1 per cent of particles hence such NFW fit is practically not possible.

The bottom panel of Fig. 1 shows the w_p for the OUTER RIM mock catalogues. The black empty points show the measurement from the eBOSS sample with jackknife errors. The various coloured lines represent the projected correlation function measured from the mock catalogues. The solid lines are for HMQ models and the dashed lines for SHOD models. The details of the different models are given in Table 3. Note that the w_p at small scales is slightly underestimated. This is probably because we did not try to fit these scales and can easily be modified by allowing additional degrees of freedom to the satellite galaxies.

In Avila et al. (2020), there is a full account of all the mock catalogues produced with the SFHOD model and further variations. In this paper, we only show the full analysis done on a subsample of SFHOD models, which complements and enhances the parameter space covered by the SHOD and HMQ models. We refer the reader to Avila et al. (2020), in particular the appendix B there, for further details. These mocks were produced by fitting the measurements of the projected correlation function and multipoles of the 3D correlation function corrected for the fibre collisions that impact the small scales of the eBOSS ELG sample. The correction was obtained using pair-wise inverse probability weight (Bianchi & Percival 2017; Mohammad, Percival & Seo 2020) method. We refer to Avila et al. (2020) for details of how the parameters of the models were obtained. Table 4 describes the details of, a subset of SFHOD models has been fitted to reproduce the observed statistics, used in this work.

7.3 RSD results

In this section, we show the results of fitting the MultiDark and the OUTER RIM mocks with the two RSD models introduced in Section 3, the TNS model (Fourier space) and the CLPT–GSRSD model (configuration space). The analysis in Fourier and configuration space is performed as described in Section 5. We note that in this paper we assume the fiducial cosmology of the mocks to be completely known and, hence, we ignore the impact that differences in fiducial cosmologies have on the results. The impact of small deviations from the fiducial cosmology on the RSD model has been discussed in our companion papers extensively (Bautista et al. 2020; de-Mattia et al. 2020; Gil-Marin et al. 2020) and shown to be small compared to the precision of our tests. We discuss the results of fitting the non-blind mocks in the following subsections.

7.3.1 MultiDark mocks

The results of RSD fits to MultiDark mocks is given in Table 5. Fig. 3 shows the results of RSD fits to the MultiDark mocks for the two RSD models considered in this paper. The top, middle, and bottom panels show $f\sigma_8$, $\alpha_{\parallel}$, and $\alpha_{\perp}$, respectively. The x-axis shows the model number as detailed in Table 3. The magenta points correspond to the TNS model in Fourier space, and the cyan points correspond to the CLPT–GSRSD model in configuration space. The filled points are fit to HMQ models for ELG, whereas the empty circles denote the fit to SHOD models for ELG. The error bars correspond to the 1σ measurement. The black-dashed line shows the true value of these parameters with 1 per cent bands being shown in grey. We find that both the RSD models (TNS and CLPT–GSRSD) with the fiducial choices are in good agreement with the truth. Model numbers 2 and 3 that have significantly different small-scale clustering of satellite and model numbers 4 and 5 that have significantly different velocity dispersion of satellite galaxies do not affect the parameters obtained using the TNS and CLPT models. Another interesting question one could ask is that what is the impact on clustering if the central galaxies are situated away from the centre of the dark matter haloes. The measurements from model 6, which has central galaxies away from the centre of the halo, do not show any significant bias. We consider three different kind of assembly bias in model numbers 7, 8, and 9 and find that the RSD models using large scales are again insensitive to the presence of such assembly bias in the galaxy catalogue. We also note that models numbers 10 and 11, which have a modified growth rate, can also be recovered by both RSD models without any significant bias. This has interesting confirmation that if the Universe is the same as ΛCDM model except that the growth rate is 20 per cent higher (lower) then a survey with 10 per cent statistical precision will be able to detect such effect with the models used here. In most models with MultiDark simulation, the parameter $\alpha_{\perp}$ seems

Table 5. Results of the redshift space distortions analysis performed on MultiDark mocks. The first set of results are for mock catalogues from the HMQ model and the second set of columns are for SHOD models. The numbers shows the best-fitting values and errors in the 2 least significant digits are shown in brackets. The expected values for $\alpha_{\rm II}$ and $\alpha_{\perp}$ are 1 for all models. The expected values for $f\sigma_8$ is 0.46 for models number 1–9, 0.55 for model number 10 and 0.37 for model number 11. We show results for both the Fourier space analysis with the TNS model and the configuration space analysis with the CLPT model.

	HMQ						SHOD					
	$P_\ell^{\rm TNS}$			$\xi_\ell^{\rm CLPT}$			$P_\ell^{\rm TNS}$			$\xi_\ell^{\rm CLPT}$		
Model	$f\sigma_8$	$\alpha_{\rm II}$	$\alpha_{\perp}$	$f\sigma_8$	$\alpha_{\rm II}$	$\alpha_{\perp}$	$f\sigma_8$	$\alpha_{\rm II}$	$\alpha_{\perp}$	$f\sigma_8$	$\alpha_{\rm II}$	$\alpha_{\perp}$
1	0.462(29)	1.023(33)	0.988(18)	0.434(48)	1.018(33)	0.975(28)	0.451(28)	1.009(32)	0.975(18)	0.451(40)	0.996(25)	0.976(24)
2	0.455(30)	1.024(35)	0.978(18)	0.444(48)	1.003(31)	0.960(28)	0.473(28)	0.975(30)	0.979(19)	0.440(44)	1.000(28)	0.965(29)
3	0.465(29)	1.022(31)	0.992(18)	0.426(46)	1.026(27)	0.961(26)	0.470(27)	0.993(33)	0.978(17)	0.469(42)	0.995(28)	0.956(26)
4	0.450(29)	1.008(32)	0.977(19)	0.447(48)	0.994(34)	0.975(31)	0.443(27)	1.011(30)	0.966(17)	0.450(41)	0.988(25)	0.975(24)
5	0.477(30)	0.999(35)	0.976(19)	0.470(50)	0.989(35)	0.970(36)	0.485(27)	1.015(34)	0.996(17)	0.473(46)	0.999(28)	0.976(28)
6	0.459(29)	0.990(33)	0.970(17)	0.429(47)	1.003(29)	0.956(25)	0.476(29)	0.986(32)	0.966(20)	0.453(43)	0.982(27)	0.964(26)
7	0.451(29)	1.022(34)	0.979(17)	0.458(48)	0.996(32)	0.979(27)	0.466(28)	1.013(31)	0.991(18)	0.444(45)	1.014(31)	0.978(28)
8	0.462(28)	1.010(32)	0.978(18)	0.444(43)	0.998(26)	0.979(24)	0.461(28)	0.994(29)	0.967(17)	0.445(41)	0.989(24)	0.966(21)
9	0.458(28)	1.005(32)	0.970(16)	0.429(45)	1.009(28)	0.965(24)	0.469(28)	1.019(31)	0.992(16)	0.448(39)	0.999(24)	0.976(23)
10	0.553(29)	1.010(29)	0.984(16)	0.527(47)	1.005(28)	0.966(25)	0.564(32)	1.019(31)	0.989(18)	0.547(43)	1.004(29)	0.973(26)
11	0.348(30)	1.020(42)	0.979(18)	0.373(47)	0.992(29)	0.984(23)	0.375(30)	0.998(38)	0.983(20)	0.353(43)	1.001(27)	0.975(26)

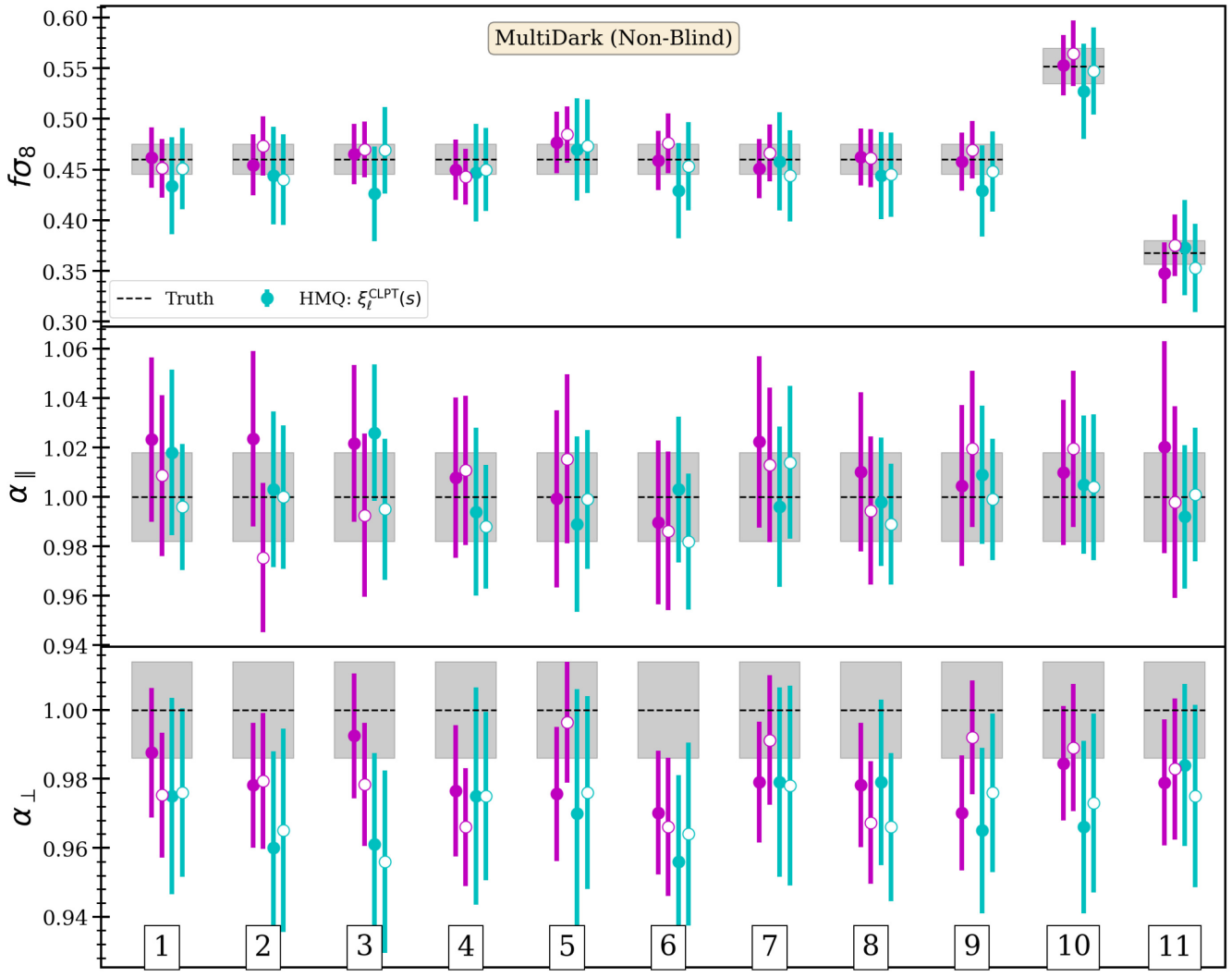

Figure 3. Results of the RSD fits to the MultiDark mocks. The three panels represents the parameters $f\sigma_8$, $\alpha_{\rm II}$, and $\alpha_{\perp}$ in the top, middle and bottom panels, respectively. The x-axis shows the model number as detailed in Table 3. The magenta and cyan points correspond to the TNS and CLPT models, respectively. The filled and empty points correspond to the HMQ and SHOD models for ELG. The error bars correspond to the 1σ measurement uncertainty. The black-dashed lines show the true value of these parameters with 1 per cent bands shown in grey.

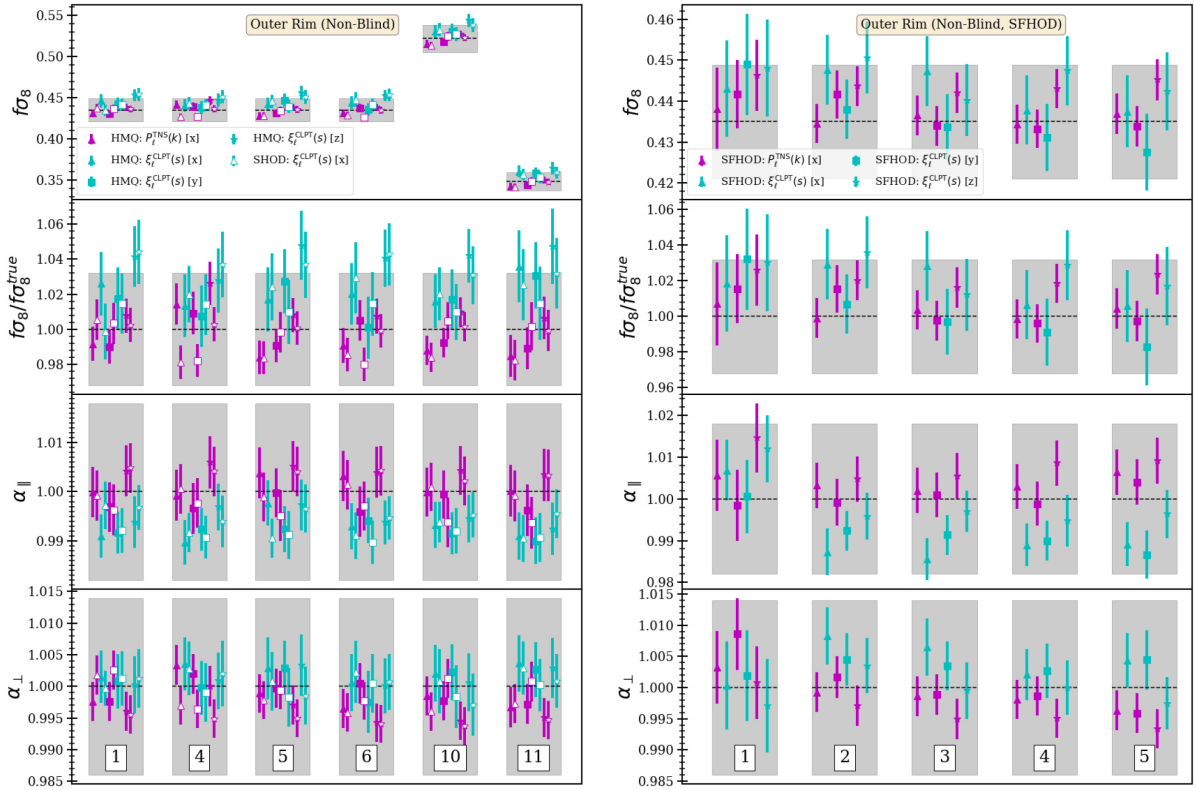

Figure 4. Results of the RSD fits to the OUTER RIM non-blind mocks. The left figure presents the SHOD and HMQ models while the right figure presents SFHOD models. The four panels in each figure represents, from top to bottom, the parameters $f\sigma_8$, $f\sigma_8/f\sigma_8^{\rm true}$, $\alpha_{\rm ||}$, and $\alpha_\perp$. The x-axis shows the model number as detailed in Tables 3 and 4. The magenta and cyan points correspond to the TNS and CLPT models, respectively. In the left figure, the filled and empty points correspond to the HMQ and SHOD models for ELGs. The error bars correspond to the 1σ measurement. The black-dashed line shows the true value of these parameters with the grey-shaded region showing the systematic error proposed in this work.

to be underestimated by $1\sigma-1.5\sigma$. We do not detect any systematic bias in the growth rate and AP scaling parameters at the level of the statistical errors of these mocks. The measurement uncertainity for these mock is a factor of 2 smaller than expected eBOSS ELG sample. But the detection of bias at high precision is not possible due to small volume (1 (Gpc/h)^3) of these mocks. A more precise test for any bias in RSD models is performed using the OUTER RIM mocks.

7.3.2 *OUTER RIM mocks*

Fig. 4 shows the results of the RSD fits to the OUTER RIM mocks for the two RSD models considered in this paper. The left figure presents the SHOD and HMQ models and the right figure SFHOD models. The four panels in each figure presents, from top to bottom, the parameters $f\sigma_8$, $f\sigma_8/f\sigma_8^{\rm true}$, $\alpha_{\rm ||}$ and $\alpha_\perp$. The x-axis in this figure shows the model number as detailed in Table 3 and 4. The magenta points correspond to the TNS model in Fourier space and the cyan points to the CLPT–GSRSD model in configuration space. In the left figure, the filled symbols show the fit of HMQ models to ELGs and the empty points show the fit of SHOD models. The error bars corresponds to the 1σ measurement. The black-dashed line shows the true value of these parameters with the grey-shaded region showing the systematic error proposed in this work. The large volume of these mocks (27 (Gpc/h)^3) results in very small statistical uncertainties. The statistical errors in these mocks is less than 2 per cent for $f\sigma_8$ and less than 1 per cent for $\alpha_{\rm ||}$ and $\alpha_\perp$. We find that both RSD models (TNS and CLPT–GSRSD) with the fiducial cosmological choices are in good agreement with the truth at the level of the statistical precision of these mocks. The uncertainity in these mocks is about $1/10^th$ of the eBOSS ELG sample, hence this should provide a reliable estimate of theoretical systematic errors for the purpose of the eBOSS ELGs sample.

It is interesting to ask whether baryonic effects can bias such cosmological measurements when performed at per cent level. There are several different ways in which baryonic physics can impact the galaxy samples. Several aspects of the complex baryonic processes can lead to incomplete sample of ELG galaxies compared to a mass-selected sample. This can be related to galaxy quenching, expulsion of cold gas from hot haloes, outflows from AGNs, supernovae events, etc. Therefore, the lack of systematic biases in the measured parameters in SHOD versus HMQ model (which encapsulate the mass incompleteness in a different way) is a remarkable success of TNS and CLPT–GSRSD model. This indicates that despite the details on how the mass incompleteness is modelled affecting the small-scale clustering, the RSD models when using relatively large scales can provide unbiased measurements of the cosmological parameters at a per cent level. The effects of various dynamical process can possibly increase or decrease the velocity dispersion of satellites. Model numbers 4 (i.e. SHOD4, HMQ4) and 5 (i.e. SHOD5, HMQ5) test for such effects and show no significant bias in the RSD parameters. Another additional feature, the observed galaxy catalogue may have, is that the central galaxies are shifted from the centre of the dark matter haloes. Model number 6 (i.e. HMQ6 and SHOD6) aims to mimic this effect and RSD fits are again unbiased.

Table 6. Result of redshift space distortions analysis on OUTER RIM mocks from the SHOD and HMQ models. The first set of results are for mock catalogue with HMQ model and second set of columns are for SHOD models. The numbers show the best-fitting values and errors in the least significant digit are shown in bracket. The expected value for $\alpha_{\rm II}$ and $\alpha_{\perp}$ is 1 for all models. The expected value for $f\sigma_8$ is 0.435 for models number 1-9, 0.522 for model number 10 and 0.348 for model number 11. We show results for both the Fourier space analysis done with the TNS model and the configuration space analysis done with the CLPT model. The *x*, *y*, *z* in the model name correspond to the same mock with line of sight for redshift space distortions along *x*-, *y*-, and *z*-axes, respectively.

	HMQ						SHOD					
		$P_\ell^{\rm TNS}$			$\xi_\ell^{\rm CLPT}$			$P_\ell^{\rm TNS}$			$\xi_\ell^{\rm CLPT}$	
Model	$f\sigma_8$	$\alpha_{\rm II}$	$\alpha_\perp$	$f\sigma_8$	$\alpha_{\rm II}$	$\alpha_\perp$	$f\sigma_8$	$\alpha_{\rm II}$	$\alpha_\perp$	$f\sigma_8$	$\alpha_{\rm II}$	$\alpha_\perp$
1x	0.431(4)	1.000(5)	0.998(3)	0.446(7)	0.991(4)	1.002(4)	0.437(5)	0.999(5)	1.002(3)	0.435(6)	0.997(4)	1.000(2)
1y	0.431(4)	0.997(5)	0.998(3)	0.443(7)	0.992(4)	1.001(4)	0.436(5)	0.996(5)	1.003(3)	0.441(7)	0.992(4)	1.001(4)
1z	0.438(4)	1.004(5)	0.996(3)	0.453(7)	0.994(5)	1.000(4)	0.436(4)	1.005(5)	0.996(3)	0.454(7)	0.997(4)	1.001(4)
4x	0.441(5)	0.999(5)	1.003(3)	0.441(7)	0.990(4)	1.004(4)	0.427(4)	1.001(4)	0.997(3)	0.444(7)	0.992(4)	1.003(4)
4y	0.439(5)	0.997(5)	1.002(3)	0.438(7)	0.992(4)	1.000(4)	0.427(4)	0.998(5)	0.996(3)	0.441(7)	0.991(4)	0.999(4)
4z	0.446(5)	1.006(5)	1.000(3)	0.447(7)	0.997(4)	1.001(4)	0.436(4)	1.004(5)	0.995(3)	0.451(8)	0.994(5)	1.002(5)
5x	0.428(4)	1.004(5)	0.999(3)	0.442(7)	0.998(4)	1.003(4)	0.428(4)	0.999(4)	0.998(2)	0.446(8)	0.991(3)	1.001(4)
5y	0.431(4)	1.000(4)	1.000(3)	0.447(7)	0.992(4)	1.003(4)	0.434(5)	0.995(5)	0.999(3)	0.439(7)	0.991(4)	0.998(4)
5z	0.439(4)	1.005(5)	0.997(3)	0.456(8)	0.997(5)	1.003(4)	0.435(4)	1.004(5)	0.995(3)	0.451(8)	0.997(4)	0.999(4)
6x	0.431(4)	1.003(5)	0.996(3)	0.444(7)	0.993(4)	1.001(4)	0.429(4)	1.001(5)	0.996(3)	0.448(8)	0.991(4)	1.002(4)
6y	0.437(5)	0.996(5)	1.001(3)	0.435(7)	0.994(4)	0.998(4)	0.426(4)	0.997(4)	0.998(3)	0.441(7)	0.990(4)	1.000(4)
6z	0.438(4)	1.004(5)	0.994(3)	0.453(7)	0.994(4)	1.000(4)	0.435(4)	1.004(5)	0.994(2)	0.454(7)	0.995(4)	1.001(4)
10x	0.516(4)	1.000(4)	0.998(3)	0.530(8)	0.993(4)	1.002(4)	0.514(4)	1.001(4)	0.996(3)	0.533(7)	0.994(4)	1.001(5)
10y	0.518(4)	0.999(4)	0.998(3)	0.531(8)	0.992(4)	1.002(4)	0.525(5)	0.994(5)	1.001(3)	0.527(8)	0.992(4)	0.998(4)
10z	0.527(4)	1.004(5)	0.995(3)	0.544(7)	0.995(4)	1.001(4)	0.523(4)	1.002(4)	0.994(2)	0.538(8)	0.995(4)	0.997(4)
11x	0.343(4)	1.000(5)	0.997(3)	0.361(7)	0.991(4)	1.004(4)	0.342(4)	0.999(5)	0.997(3)	0.357(7)	0.990(4)	1.003(4)
11y	0.344(4)	0.996(5)	0.997(3)	0.359(6)	0.990(4)	1.003(4)	0.349(4)	0.994(5)	1.001(3)	0.353(7)	0.991(5)	1.000(4)
11z	0.350(4)	1.003(5)	0.995(3)	0.365(7)	0.992(5)	1.003(4)	0.348(4)	1.003(5)	0.995(3)	0.359(7)	0.996(5)	1.001(4)

The SFHOD models also show an unbiased measurement of RSD parameters (see right-hand panel of Fig. 4). The SFHOD model number 1 assumes that satellite galaxies follow a Poisson distribution whereas model numbers 2 and 3 use a negative binomial distributions with $\beta = 0.1$ and $\beta = 0.2$, respectively. The SFHOD model number 4 assumes a next integer from Poisson distribution for satellites. These models have different small-scale physics and hence different FoG effects that can arise due to baryon physics (note that a next integer distribution has been reported in SAMs, which are not directly accounting for hydrodynamical interactions). The SFHOD model number 5 introduces an infalling velocity component to satellite galaxies motivated by behaviour of model galaxies in Orsi & Angulo (2018). All of the five SFHOD models do not show any significant systematic bias in the RSD parameters beyond the statistical uncertainty of the mocks (see Fig. 4).

We have shown how the results obtained vary for each mock galaxy catalogue when projecting the RSD along different los. The scatter that is seen between the different line of sight looks consistent with the errors, and we mitigate it by averaging together the three measurements. In the mocks that are produced for the quasar sample, a much larger scatter is seen in the $f\sigma_8$ measurements for different los (Smith et al. 2020). This is investigated in more detail in Smith et al. (in preparation), where it is shown that the scatter in $f\sigma_8$ is larger for tracers with a larger linear bias. Since measurements of the quadrupole (and hence $f\sigma_8$) are anticorrelated, large gains in the precision can be made by taking the mean of the three los, which is greater than what would be expected if the volume was increased by a factor of 3.

Overall we show in Fig. 4 along with Table 6 and 7 that the way the HOD models encapsulate different baryonic physics for ELGs do not bias the RSD parameters. This is true for both TNS and CLPT–GSRSD models to few per cent precision. The RSD models are unbiased when limited to using $k_{\rm max} = 0.2\,{\rm Mpc}^{-1}\,h$ for Fourier space and $s_{\rm min} = 32\,h^{-1}\,{\rm Mpc}$ in configuration space. This is a remarkable success of the perturbation theory schemes against such wide variety of galaxy formation models along with various forms of halo mass incompleteness. This result is encouraging while looking forward to very precise measurements in the future.

Table 7. Result of redshift space distortions analysis on SFHOD mocks using the OUTER RIM simulation. We provide the best-fitting values and errors in the least significant digits are shown in bracket. Results are given for both Fourier space analysis with TNS model and configuration space analysis with CLPT model. The *x*, *y*, *z* in the model name corresponds to the same mock with line of sight for redshift space distortions along *x*-, *y*-, and *z*-axes, respectively.

		$P_\ell^{\rm TNS}$			$\xi_\ell^{\rm CLPT}$	
Model	$f\sigma_8$	$\alpha_{\rm II}$	$\alpha_\perp$	$f\sigma_8$	$\alpha_{\rm II}$	$\alpha_\perp$
1x	0.438(10)	1.006(8)	1.003(5)	0.443(11)	1.007(7)	1.000(7)
1y	0.442(8)	0.998(8)	1.009(5)	0.449(12)	1.001(8)	1.002(7)
1z	0.446(8)	1.015(8)	1.001(5)	0.448(11)	1.012(8)	0.997(7)
2x	0.435(4)	1.003(5)	0.999(3)	0.448(8)	0.987(5)	1.008(4)
2y	0.442(5)	0.999(5)	1.002(3)	0.438(7)	0.992(4)	1.005(4)
2z	0.444(4)	1.005(5)	0.997(3)	0.451(8)	0.996(5)	1.004(4)
3x	0.437(4)	1.002(5)	0.999(3)	0.447(8)	0.986(4)	1.007(4)
3y	0.434(4)	1.001(5)	0.999(3)	0.434(7)	0.991(4)	1.003(3)
3z	0.442(4)	1.005(5)	0.995(3)	0.440(8)	0.997(4)	1.000(4)
4x	0.434(4)	1.003(5)	0.998(3)	0.438(8)	0.989(5)	1.002(4)
4y	0.433(4)	0.999(5)	0.999(3)	0.431(8)	0.990(4)	1.003(4)
4z	0.443(4)	1.009(5)	0.995(3)	0.447(8)	0.995(6)	1.000(4)
5x	0.437(4)	1.006(5)	0.996(3)	0.438(8)	0.989(5)	1.004(4)
5y	0.434(4)	1.004(5)	0.996(3)	0.428(9)	0.987(5)	1.004(4)
5z	0.445(5)	1.009(5)	0.993(3)	0.442(9)	0.996(5)	0.997(4)

8 BLIND MOCK CHALLENGE

In this section, we describe the blind part of our mock challenge. The main focus of this measurement has been testing the ability of perturbation theory based RSDs models to obtain unbiased growth rate ($f\sigma_8$) measurements. Therefore, we create a new set of mocks using the OUTER RIM simulation with a blind true growth rate and

Table 8. Results of the redshift space distortions analysis on the OUTER RIM blind mocks. The first set of results are for mock catalogues from the HMQ models and the second set of columns are from SHOD models. The numbers show the best-fitting values and errors in the least significant digits are shown within bracket. We show results for both the Fourier space analysis with the TNS model and the configuration space analysis with the CLPT model. The *x*, *y*, *z* in the model name corresponds to the same mock with line of sight for redshift space distortions along *x*-, *y*-, and *z*-axes, respectively.

	HMQ						SHOD					
	$P_\ell^{\rm TNS}$			$\xi_\ell^{\rm CLPT}$			$P_\ell^{\rm TNS}$			$\xi_\ell^{\rm CLPT}$		
Model	$f\sigma_8$	$\alpha_{\rm ll}$	$\alpha_\perp$	$f\sigma_8$	$\alpha_{\rm ll}$	$\alpha_\perp$	$f\sigma_8$	$\alpha_{\rm ll}$	$\alpha_\perp$	$f\sigma_8$	$\alpha_{\rm ll}$	$\alpha_\perp$
1x	0.213(7)	0.998(8)	0.996(7)	0.219(7)	0.995(8)	1.000(7)	0.214(5)	0.998(10)	0.999(5)	0.220(4)	0.997(10)	1.001(5)
1y	0.215(6)	0.994(7)	0.997(7)	0.222(8)	0.993(10)	0.999(9)	0.214(6)	0.997(8)	0.997(7)	0.220(6)	0.995(9)	0.998(6)
1z	0.221(7)	1.002(10)	0.993(8)	0.227(8)	1.000(13)	0.996(8)	0.221(8)	1.000(11)	0.996(7)	0.227(8)	0.999(11)	0.997(8)
2x	0.322(6)	1.002(6)	0.997(7)	0.331(6)	0.997(7)	1.002(8)	0.321(5)	1.000(8)	0.997(7)	0.329(7)	0.997(8)	1.002(8)
2y	0.323(6)	0.997(6)	0.996(6)	0.331(6)	0.993(7)	1.000(7)	0.320(6)	0.998(7)	0.996(6)	0.328(7)	0.994(8)	0.998(7)
2z	0.330(7)	1.002(8)	0.994(7)	0.338(10)	0.998(9)	0.999(9)	0.331(7)	1.001(8)	0.995(7)	0.337(7)	1.000(11)	0.997(8)
3x	0.431(7)	0.999(5)	0.996(7)	0.442(7)	0.995(7)	1.003(7)	0.431(6)	1.000(6)	0.998(5)	0.440(5)	0.997(7)	1.001(5)
3y	0.431(7)	0.999(6)	0.997(6)	0.440(7)	0.993(8)	1.002(5)	0.430(7)	0.999(5)	0.998(5)	0.438(6)	0.995(6)	0.999(5)
3z	0.439(7)	1.002(7)	0.994(6)	0.448(7)	0.997(9)	0.998(5)	0.438(8)	1.002(5)	0.996(6)	0.449(6)	0.998(8)	0.999(6)

provide that to participants for analysis. The blind mocks are created by scaling the halo velocity linearly resulting in scaling of true growth rate. We create six blind mocks in this paper, three using SHOD models to populate ELGs and another three using HMQ models. These mocks are analysed using the same method and scales as for the analysis on non-blind mocks, as described in detail in Section 5. The number density for blind mocks is set to the $2 \times 10^{-4}\,h^3\,{\rm Mpc}^{-3}$, which is close to the mean number density of the eBOSS ELG sample. We have created 30 realizations for each of the three HMQ models and 40 for each of the three SHOD models. These realizations are created from the same halo catalogue but subsampling randomly a distinct set of haloes for each realization. The number of realizations is set by the total number density obtained for the full halo catalogue based on the HOD model. The error quoted in the Table 8 for the blind mocks is the scatter in the dispersion of these 30 (40) realizations for the HMQ (SHOD) models.

The six blind mocks use the same underlying halo catalogue from OUTER RIM as the non-blind mocks presented in the previous section and hence the underlying cosmological parameters were known to everyone. An analysis with blind cosmological parameters is left for the future. In this paper, we focus on the ability to constrain the growth rate, rather than the full cosmology. We generate three models for each of HMQ and SHOD ELG models using the underlying parameters given in Table 2. We scale the growth rate by 0.5 for the blind mock number 1, by 0.75 for blind mock number 2 and by 1.0 for number 3. The RSD along each of the axis of cubic box were applied as indicated in the Table 8 by *x*, *y,* and *z* with the model number. These shifts were kept blinded until we finalised all the plots and tables for this paper. The shifts in the growth rate are at 30σ and 15σ level assuming 1.6 per cent statistical uncertainty in measurement of growth rate. The shifts are set to such large values in order to study whether the model can obtain an unbiased estimate of growth rate at per cent level precision despite it being far away from the default value.

8.1 Blind mocks results

We present the result of analysing the blind mocks from OUTER RIM simulation in Figs 5 and 6. Table 8 summarizes the parameter constraints. Fig. 5 shows the results of the RSD fits using the two models TNS and CLPT. From top to bottom, the four panels represent the parameters $f\sigma_8$, $f\sigma_8/f\sigma_8^{\rm true}$, $\alpha_{\rm ll}$, and $\alpha_\perp$. The error bars corresponds to the 1σ measurement. It is clear from the top panel in Fig. 5 that our choice of blind mocks cover a wide range of growth rates. These are consistently recovered by the two RSD models with a precision close to the per cent level. The large volume of these blind mocks result in very small statistical uncertainties. The mean 1σ statistical error in growth rate are 1.6 per cent, 2.2 per cent, and 3.2 per cent for model number 3, 2, and 1, respectively (see Table 8). The mean 1σ statistical errors for $\alpha_{\rm ll}$ is 0.9 per cent and for $\alpha_\perp$ is 0.7 per cent. We note that the uncertainties in the configuration space analysis using CLPT are fairly close to those obtained in Fourier space using the TNS model. We also note that the mean deviation of the parameters measured from the true values is [0.6, 0.2, 0.6] $\times\,\sigma_{\rm stat}$ for $f\sigma_8$, $\alpha_{\rm ll}$, and $\alpha_\perp$, respectively, for the TNS model, whereas the configuration space analysis results in mean deviation of [0.9, 0.4, 0.2] $\times\,\sigma_{\rm stat}$ for $f\sigma_8$, $\alpha_{\rm ll}$, and $\alpha_\perp$,m, respectively. We also note that the statistical errors for the blind mocks are probably slightly underestimated given they are coming from a small number of realizations sampled from the same halo catalogue. Therefore, we do not detect any systematic bias in the blind mock challenge for the TNS and CLPT models at the statistical precision of these mocks. Note that this remarkable success of the TNS and CLPT models might be partially driven by the fact that we kept a conservative cut in scale to limit the impact of non-linear growth of dark matter and baryonic physics on our measurements. It remains to be seen how far one can push in non-linear scales when analysing the mocks with one-tenth of the statistical error used in this work as this will be the typical requirement of future surveys.

In order to illustrate the accuracy and success of the RSDs models, we show measurements from the blind mocks along with the best-fitting models in Fig. 6. The top panel shows the power spectrum multipoles and the bottom panel is for the correlation function ones. The measurements from the mocks along with their error are shown with the circles, whereas the best-fitting models are shown with the lines. The mocks from models with quenching (i.e. HMQ) are shown with the filled symbols and those from models without quenching (i.e. SHOD) are shown with the empty symbols. The solid, dashed, and dot–dashed lines are for Legendre moments with $\ell = 0$, $\ell = 2$, and $\ell = 4$, respectively. The power spectrum uses TNS, whereas the correlation function uses CLPT–GSRSD to model the RSDs. The SHOD blind model number 1, 2, and 3 are shown with the blue, cyan, and orange colours, respectively, whereas HMQ blind model number 1, 2, and 3 are shown with the magenta, red, and purple colours, respectively. For the model to work, the same coloured line (best fit from theory) should go through the same coloured points (measurements from the blind mocks). Taking this into account, we can conclude that both models describe the blind mocks remarkably successfully.

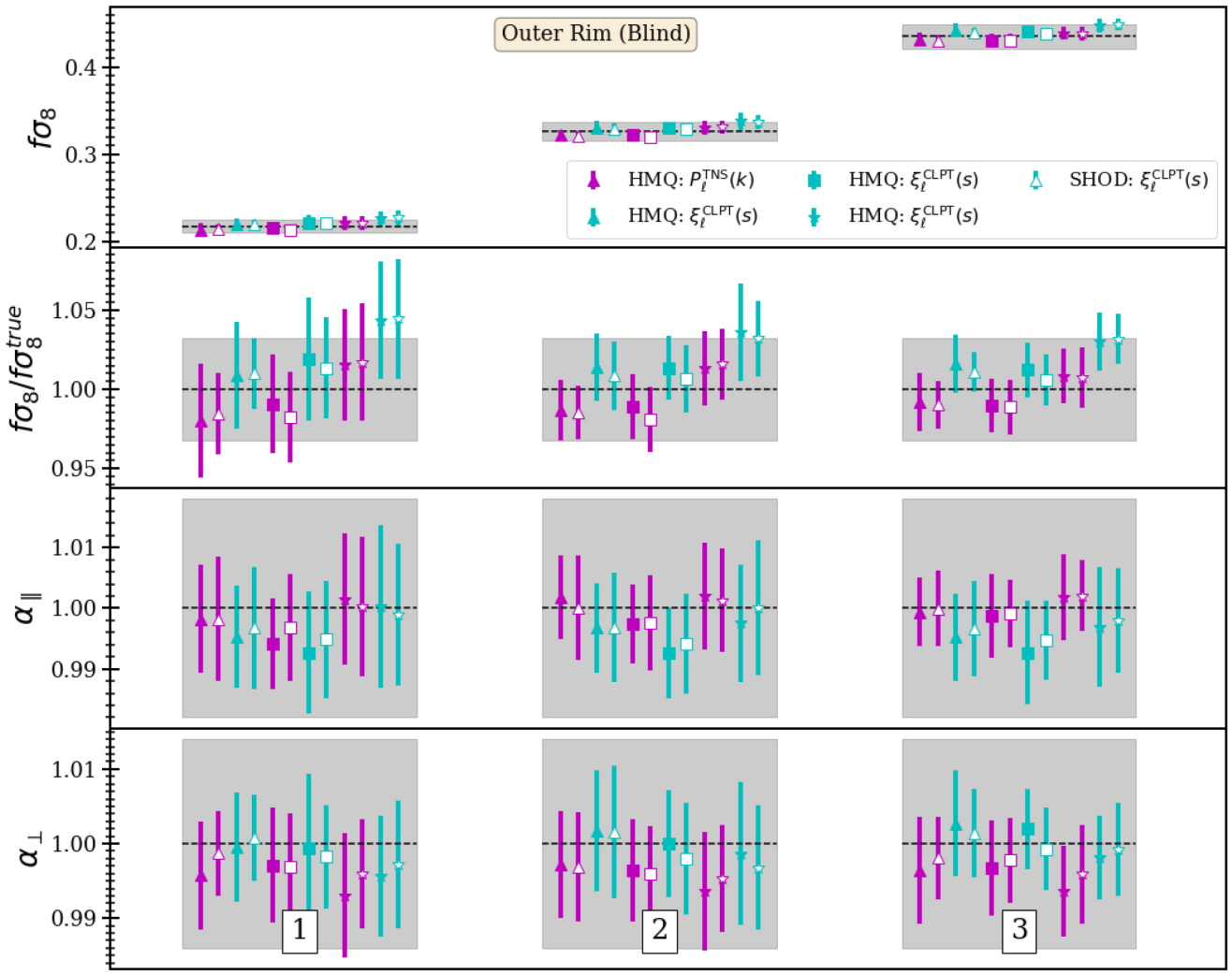

Figure 5. Results of RSD fits to the OUTER RIM blind mocks. From top to bottom, the four panels presents the parameters $f\sigma_8$, $f\sigma_8/f\sigma_8^{\rm true}$, $\alpha_{\rm ||}$, and $\alpha_\perp$. The x-axis shows the three different blind models with the traingle, the square, and the star marker for RSD realizations along x-, y-, and z-axes, respectively (see Table 8 for values). The magenta and cyan points correspond to the TNS and CLPT models, respectively. The filled and empty points correspond to the HMQ and SHOD models for ELGs. The error bars correspond to the 1σ measurement uncertainty. The black-dashed lines show the true value of these parameters with the grey-shaded region showing the systematic error proposed in this work. It is clear from the top panel that our choice of blind mocks cover a wide range of growth rate which is consistently recovered by the two RSD models.

9 SYSTEMATIC ERRORS

The final aim of this paper is to provide the theoretical systematic uncertainties related to the modelling of the clustering of the eBOSS ELG sample. Therefore, we provide estimates of systematic error in the measurements of $f\sigma_8$, $\alpha_{\rm ||}$, and $\alpha_\perp$ for the TNS model in Fourier space and the CLPT model in configuration space. This systematic error asses the impact of galaxy formation physics. In particular we consider impact of quenching mechanism, assembly bias, in falling of satellite galaxies, satellites having different concentration and velocity dispersion compared to dark matter through various mock catalogues.

We measure three quantities for each of the RSD parameters $f\sigma_8$, $\alpha_{\rm ||}$, and $\alpha_\perp$, and type of HOD model described in Section 6 to asses the systematic bias, as given below:

$$\mu_{\rm sys} = \langle |x - x_{\rm true}| \rangle \ , \tag{24}$$

$$\sigma^2_{\rm sys} = \left\langle (x - x_{\rm true})^2 \right\rangle - \langle x - x_{\rm true} \rangle^2 \ , \tag{25}$$

$$\sigma_{\rm stat} = \text{statistical error from fit} \ . \tag{26}$$

Above, x represents one of the RSD parameters (i.e. $f\sigma_8$, $\alpha_{\rm ||}$, $\alpha_\perp$) and averages are taken over all the mocks in a given type of HOD model. The parameter $\mu_{\rm sys}$ represents the mean systematic shift from the true value, $\sigma_{\rm sys}$ represents the rms of the systematic shift, and $\sigma_{\rm stat}$ represents the statistical error. We consider a systematic bias is significant only if $\mu_{\rm sys} > 2\sigma_{\rm stat}$. Assuming Gaussian statistics for the systematic errors, this requirement implies that we only detect a systematic bias if statistically there is only a 5 per cent chance to explain the distance from the measured parameter to the truth.

The measurement of these three parameters ($\mu_{\rm sys}$, $\sigma_{\rm sys}$, $\sigma_{\rm stat}$) is shown in Fig. 7 and given in Table 9. Table 9 lists the systematic error in each of the three RSD parameters for the two RSD models, TNS and CLPT, and four different HOD model categories, SHOD, HMQ, SFHOD, and Blind (all of the Blind models) based on the OUTER RIM simulation. We do not provide these values for mocks based on the MultiDark simulation as the statistical errors in those

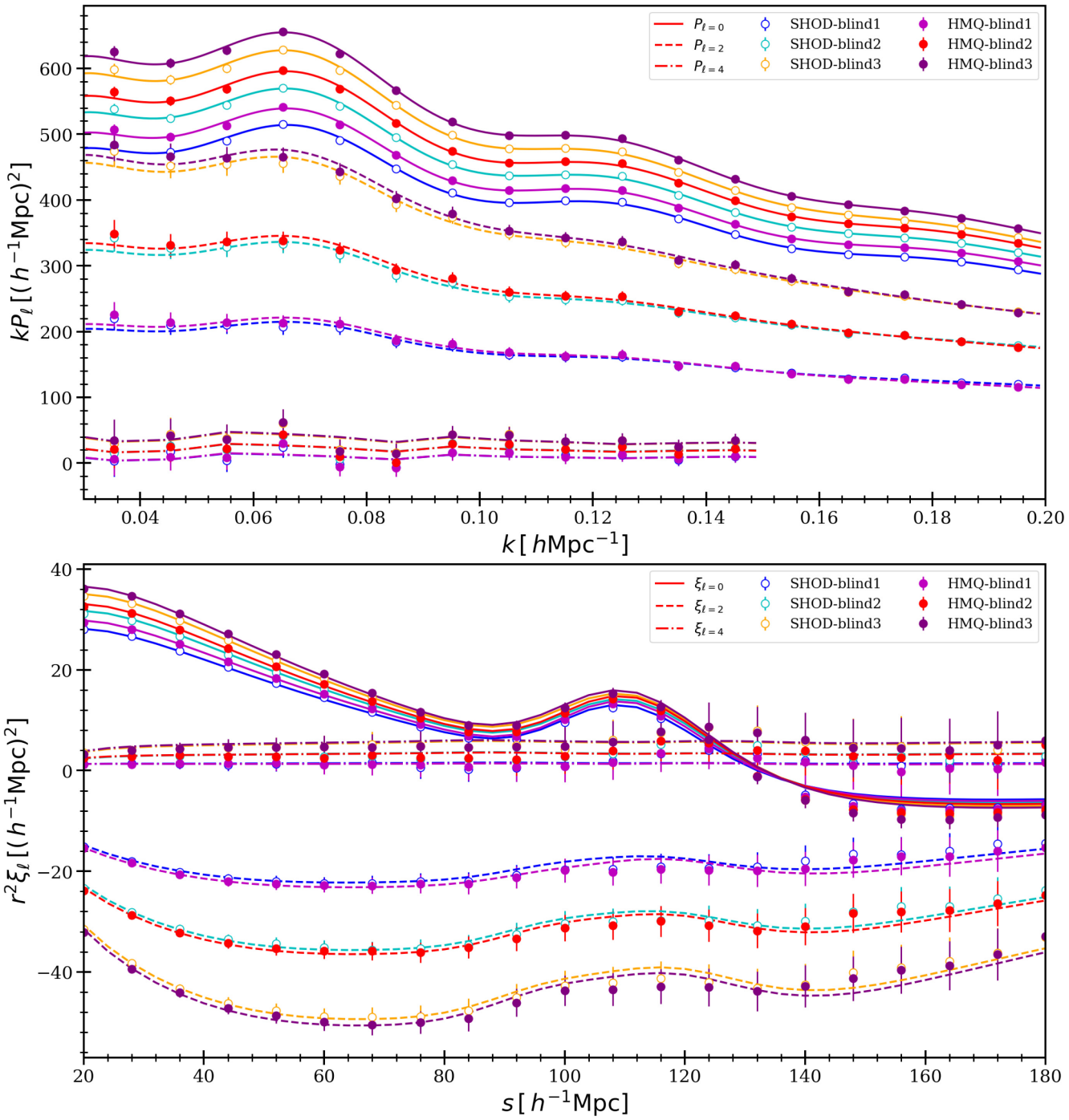

Figure 6. Clustering measurement for the blind mocks along with the best-fitting models. The top panel shows the power spectrum multipoles and the bottom panel the correlation function multipoles. The measurements from the mocks along with their error are shown with the circles, whereas the best-fitting models are shown with the lines. The mocks from the model with quenching (i.e. HMQ) are shown with the filled symbols and those from the model without quenching (i.e. SHOD) are shown with the empty symbols. The solid, dashed, and dot–dashed lines are for the Legendre moments with $\ell = 0$, $\ell = 2$, and $\ell = 4$ respectively. The power spectrum uses TNS, whereas the correlation function uses CLPT–GSRSD to model the redshift space distortions. Both models describe the mocks remarkably successfully.

are much larger. The systematic shift ($\mu_{\rm sys}$) for the TNS model in $f\sigma_8$ is 0.004, 0.005, 0.005, and 0.004 for the SHOD, HMQ, SFHOD, and Blind mocks, respectively. These systematic shifts are either smaller or at the level of the statistical errors. Although $\mu_{\rm sys}$ for the CLPT model in $f\sigma_8$ for SHOD (0.01) and HMQ (0.011) is slightly larger than the statistical errors, this difference is not statistically significant. The systematic shift ($\mu_{\rm sys}$) for the TNS model in $\alpha_{\shortparallel}$ and $\alpha_\perp$ is always smaller than the corresponding $\sigma_{\rm stat}$ for all the four mocks, except for $\alpha_\perp$ in SHOD model. The systematic shift for the CLPT model in $\alpha_\perp$ is smaller than $\sigma_{\rm stat}$ for all four mocks but the one in $\alpha_{\shortparallel}$ are larger than $\sigma_{\rm stat}$. But this shift in $\alpha_{\shortparallel}$ does not cross our requirement of significant systematic(i.e. $\mu_{\rm sys} > 2 \times \sigma_{\rm stat}$).

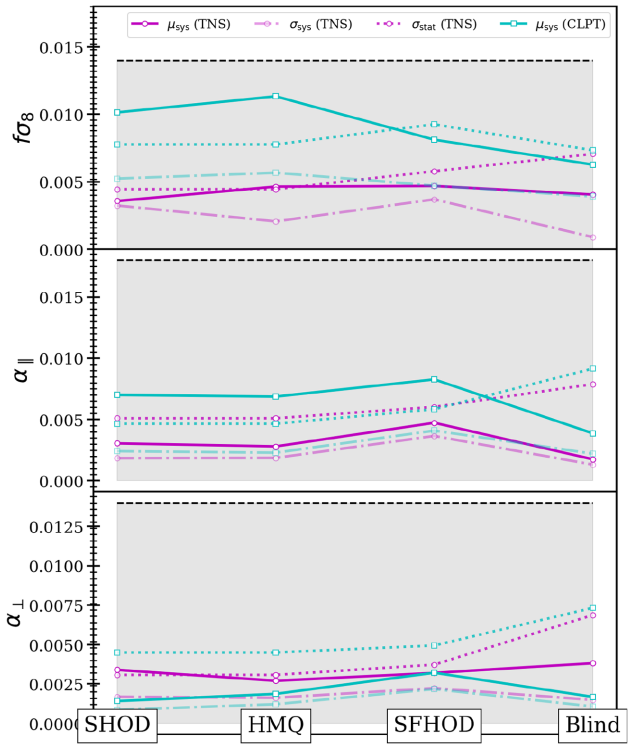

Figure 7. Comparison of systematic and statistical absolute errors for $f\sigma_8$ (top), $\alpha_{||}$ (middle), and $\alpha_\perp$ (bottom). The x-axis shows the results for different kind of mocks. In each panel, the solid line is for μ_{sys} representing mean systematic shift, the dot–dashed line is for σ_{sys} representing the rms of mean systematic shift from true values of the parameter, and the dashed line is for σ_{sys} representing statistical errors. The magenta colour is for the TNS model and the cyan colour for CLPT. The shaded region with the black-dashed line shows the theoretical systematic error proposed in this work. We note that a detection of systematic bias as per our definition will mean that the coloured solid lines above twice the value of the corresponding coloured dashed lines. Therefore, this figure illustrates that for both RSD model and all four type of mock catalogues we do not detect any systematic bias.

The numbers given in Table 9 for the systematic errors can be visualized in Fig. 7. The top, middle, and bottom panels in this plot correspond to the absolute errors for $f\sigma_8$, $\alpha_{||}$, and $\alpha_\perp$ respectively. The x-axis shows the results for different categories of mocks as indicated at the bottom panel. In Fig. 7, the solid lines are for μ_{sys}, the mean systematic shift, dot–dashed lines are for σ_{sys}, the standard deviation of mean systematic shift, and the dotted lines are for σ_{stat}, the statistical errors. The magenta colour shows results from the power spectrum analysis using the TNS model and the cyan colour shows results from the correlation function analysis using the CLPT model. In this work, only the solid lines above twice the value of the dotted lines do imply the existence of a significant systematic bias. Therefore, Fig. 7 illustrates that for both RSD models and all four categories of mock catalogues we do not detect any systematic bias.

The error in the three RSD parameters for blind mocks is fairly close between the Fourier space analysis using TNS and the configuration space analysis using CLPT. We remind readers that the Fourier space analysis uses $k_{max} = 0.2$, whereas the configuration space analysis uses $s_{min} = 32$. The two scale cuts are equivalent if we related the Fourier conjugates as $k_{max} = 2\pi/s_{min}$. Hence, the two analysis shows similar level of information from the two-point clustering of galaxies.

Table 9. Estimate of systematic and statistical errors in the three RSD parameters $f\sigma_8$, $\alpha_{||}$, and $\alpha_\perp$. The first three columns are from power spectrum measurements using the TNS model, whereas the second set of columns are from the correlation function measurements using the CLPT model. The subtables are for different ELG models, from top to bottom: SHOD, HMQ, SFHOD, and Blind models. The quantity μ_{sys} represent the mean bias, σ_{sys} represent the rms in the mean bias, and σ_{stat} represent the statistical error. The values in the table are in units of 10^3. We consider that there is a significant systematic bias when $\mu_{sys} > 2\sigma_{stat}$. Note that all values reported in this table are absolute errors on the parameters and not percentage errors.

	P_ℓ^{TNS}			ξ_ℓ^{CLPT}		
$\times 10^3$	$f\sigma_8$	$\alpha_{||}$	$\alpha_\perp$	$f\sigma_8$	$\alpha_{||}$	$\alpha_\perp$
SHOD						
μ_{sys}	3.6	3.0	3.4	10.1	7.0	1.4
σ_{sys}	3.2	1.8	1.7	5.2	2.4	0.8
σ_{stat}	4.4	5.1	3.1	7.8	4.7	4.5
HMQ						
μ_{sys}	4.6	2.8	2.7	11.3	6.9	1.9
σ_{sys}	2.1	1.9	1.6	5.7	2.3	1.2
σ_{stat}	4.4	5.1	3.1	7.8	4.7	4.5
SFHOD						
μ_{sys}	4.7	4.7	3.2	8.1	8.3	3.2
σ_{sys}	3.7	3.7	2.2	4.7	4.1	2.2
σ_{stat}	5.8	6.0	3.7	9.3	5.8	4.9
Blind						
μ_{sys}	4.0	1.7	3.8	6.3	3.9	1.7
σ_{sys}	0.9	1.3	1.5	3.9	2.2	1.1
σ_{stat}	7.1	7.9	6.9	7.3	9.2	7.3

We take a conservative choice and suggest using twice the statistical error in the blind mocks as the theoretical systematic. We propose the following theoretical systematic errors, common to the two RSD models, TNS and CLPT: 0.0146 for $f\sigma_8$, 0.0184 for $\alpha_{||}$, and 0.0146 for $\alpha_\perp$. This results in a theoretical systematic error budget of 3.3 per cent, 1.8 per cent, and 1.5 per cent in $f\sigma_8$, $\alpha_{||}$ and $\alpha_\perp$, respectively. These are approximately twice of the errors obtained for the blind mock and taken a maximum over the two RSD models as given in Table 9. We would like to emphasize that these systematic errors are very conservative and are not a reflection of the limits of two RSD models but rather they reflect the limits of the tests performed in this work. In fact, the two RSD models (CLPT and TNS) are found to be unbiased at the precision of the results in this paper.

10 CONCLUSIONS

Galaxy redshift surveys (e.g. Percival et al. 2004; Schlegel et al. 2009; Blake et al. 2011; Beutler et al. 2012; de la Torre et al. 2013; Liske et al. 2015; Dawson et al. 2016) measure 3D positions of millions of galaxies in redshift space. This allows us to measure the clustering of galaxies in redshift space in the late time Universe, and hence, to probe the cosmological growth at the epoch of the galaxy sample. Such measurement requires predicting the measured clustering in order to obtain constraints on the parameters of interest. But in principle this would require understanding galaxy physics to be able to predict the galaxy clustering at very high precision, which is a very hard and highly non-linear problem. Therefore, the models often take a perturbative approach to solve the clustering of the dark matter and then perform another perturbative expansion of the galaxy formation process in terms of galaxy bias. Such solutions are expected to work very well on linear scales and for mass selected complete samples of galaxies. When we start observing a wide varity

of galaxies that might be highly influenced by their environment then such perturbative approach needs to be tested rigorously to avoid erroneously biased measurement of properties of the Universe.

In this paper, we focus on the eBOSS ELG (i.e. star-forming galaxy) sample (Raichoor et al. 2020). eBOSS ELGs have relatively lower mass galaxies (Gonzalez-Perez et al. 2018; Guo et al. 2018; Alam et al. 2019) compared to LRGs studied in the past Alam et al. (2017b). The eBOSS ELG sample is analysed in Fourier space using the TNS model (de-Mattia et al. 2020) and in configuration space using the CLPT model (Tamone et al. 2020) for RSDs. In this paper, we test these models, close to per cent level precision, for the existence of any systematic bias due to theoretical approximations taken in the perturbative approach and simplistic ways to model the galaxy formation effects. This is the first tests being done at such high precision for these RSD models focusing on ELGs. This work should be considered as the first step towards testing of models for future surveys such as DESI (DESI Collaboration 2016) and PFS (Takada et al. 2014b), which will be dominated by star-forming ELGs. Similar studies have been performed in companion papers focusing on the eBOSS QSOs sample (Smith et al. 2020) and eBOSS LRG sample (Rossi et al., in preparation).

We use high-resolution N-body simulations, MultiDark and OUTER RIM, to obtain halo catalogues at the mean effective redshift ($z = 0.86$) of the eBOSS ELGs sample. Such halo catalogue creates a fully non-linear realization of the dark matter field, which is the first essential ingredient of the Universe. We then populate the halo catalogues with a range of HOD models. We use three different parametrizations for the shape of the mean HOD of central galaxies. The first parametrization, SHOD, is the standard HOD that ignores existence of any galaxy quenching at the centre of massive haloes and is more appropriate for modelling magnitude or stellar mass selected samples (Zheng et al. 2005; White et al. 2011). But we do allow the normalization of the central occupation to be free to account for incompleteness of ELG in high mass dark matter haloes. The second HOD parametrization, HMQ, that encapsulates the quenching of the star formation in galaxies at the centre of massive haloes, and hence should provide a more realistic realization of star-forming ELGs (Alam et al. 2019). The third HOD parametrization, SFHOD, is based on the results for ELGs from a SAM of galaxy formation and evolution (Gonzalez-Perez et al. 2018; Avila et al. 2020). In each of these HOD models, we introduce parameters to account for other various baryonic effects that can affect the spatial distribution of satellite galaxies, their dynamical properties, including infalling velocities, assembly bias, off centring in the location of central galaxies and deviations in large-scale velocities.

We first create a set of non-blind mock catalogues, for which all the parameters of the mocks were available to the teams analysing them. We then analyse these non-blind mock based on MultiDark and OUTER RIM using the TNS model in Fourier space and the CLPT model in configuration space. For the mocks based on the MultiDark simulation, illustrative power spectrum are shown in Fig. 2, the result of the RSD analysis is shown in Fig. 3 and the parameters constraints are given in Table 5. We note that fig. 2 highlights that the impact of galaxy physics on the galaxy power spectrum can be up to 10 per cent by $k \approx 0.2$ (scales analysed in this paper). The MultiDark mocks have a volume of $1(\mathrm{Gpc/h})^3$ and hence have statistical errors of 8 per cent, 3 per cent, and 2 per cent in $f\sigma_8$, $\alpha_{\shortparallel}$, and $\alpha_{\perp}$, respectively. We do not detect any significant bias when analysing the MultiDark mocks with either of the RSD models. But this is a weak statement given the statistical uncertainty of these mock due to their small volume. For the non-blind mocks based on the OUTER RIM simulation, the results of the RSD analysis are shown in Fig. 4 and the parameter constraints are given in Table 6 and 7. The statistical uncertainties in the OUTER RIM mocks with volume of $27(\mathrm{Gpc/h})^3$ are 1–2 per cent, 0.5–0.6 per cent, and 0.3–0.5 per cent in $f\sigma_8$, $\alpha_{\shortparallel}$, and $\alpha_{\perp}$, respectively. We note that for OUTER RIM non-blind mocks we again do not detect any statistical significant systematic bias at the level of statistical uncertainty in these parameters despite the wide range of ELG models used.

We have analysed a wide variety of models, with a range of kinematical degrees of freedom for satellite galaxies, assembly bias, and various forms of mass incompleteness. Nevertheless, we do not span the complete parameter space of the ELG connection to the dark matter haloes and cosmic web. For example, we do not consider any model that correlates the ELG occupation with the tidal environment of dark matter haloes. Alam et al. (2019) recently showed that the ELGs slightly prefers to populate the haloes in the low-density filaments compared to the prediction of HMQ model used in this paper. But any such tidal correlation in observational data have only been detected at low significance and hence are expected to be small. Therefore, at the level of our precision we suggest that our models spans wide enough parameter space of ELG population such that we can be confident about the robustness of RSD models.

We finally create a set of blind mocks. Our focus has been to study the biases in the $f\sigma_8$ coming from theoretical approximations in the RSD models. Therefore, our mocks are blind only in the $f\sigma_8$ measurements and all other information was known to the analysis teams. We show the results of the RSD analyses from blind mocks in Fig. 5 and the constraints are shown in Table 8. We also show the comparison of mock measurements and best-fitting models for the blind mocks in Fig. 6. Based on these figures and tables, we conclude that the TNS model in Fourier space and the CLPT model in configuration space can describe the blind mock catalogues remarkably well, obtaining unbiased measurement of $f\sigma_8$.

We present the systematic error from all the mocks in Section 9. Fig. 7 presents the systematic errors and Table 9 lists their values for both the RSD models, comparing them to statistical errors for the different categories of mocks. We conclude, through these series of detailed analysis of mocks with versatile galaxy physics models, that the TNS model in Fourier space and the CLPT model in configuration space provide an unbiased measurement of RSDs within the statistical error of our mocks. Therefore, taking a conservative choice, we suggest using twice the statistical error obtained for the blind mocks as the theoretical systematic for these model unless a more precise test is performed. For both RSD models (i.e. TNS and CLPT), we propose the common theoretical systematic errors of 3.3 per cent, 1.8 per cent, and 1.5 per cent in $f\sigma_8$, $\alpha_{\shortparallel}$, and $\alpha_{\perp}$, respectively. The theoretical systematic errors proposed here are an order of magnitude smaller than the statistical error for eBOSS ELG sample (de-Mattia et al. 2020; Tamone et al. 2020) and hence are negligible for the purpose of the current eBOSS ELG analysis. We emphasize that RSDs of incomplete galaxy samples such as ELGs can be modelled with TNS ($k_{\mathrm{max}} = 0.2\,\mathrm{Mpc}^{-1}\,h$) and CLPT ($s_{\mathrm{min}} = 32\,h^{-1}\mathrm{Mpc}$) without any systematic biases to a few per cents level.

The upcoming DESI survey (DESI Collaboration 2016) will have an effective volume of $20(\mathrm{Gpc/h})^3$ for the ELG sample. This will result in statistical errors smaller than the systematic errors proposed in this paper. Hence, systematic errors can have a significant contribution to the total error budget for DESI ELGs. Therefore, one must perform a similar analysis with much smaller uncertainty and hence much bigger volume of simulations in order to avoid adding significant uncertainty from theoretical systematic to the total error budget.

ACKNOWLEDGEMENTS

SA and JAP are supported by the European Research Council through the COSFORM Research Grant (#670193). VGP acknowledges support from the European Union's Horizon 2020 research and innovation programme (ERC grant #769130) and by the Atracción de Talento Project no. 2019-T1/TIC-12702 granted by the Comunidad de Madrid in Spain. SH and KH acknowledge support under the U.S. Department of Energy contract W-7405-ENG-36 at Argonne National Laboratory. GR acknowledges support from the National Research Foundation of Korea (NRF) through grant 2017R1E1A1A01077508 and No. 2020R1A2C1005655 funded by the Korean Ministry of Education, Science and Technology (MoEST). RP and SE acknowledge support from the French National Research Agency under grants ANR-16-CE31-0021 (ANR eBOSS), ANR-11-LABX-0060 (OCEVU LABEX), and ANR-11-IDEX-0001-02 (A∗MIDEX project).

Funding for the SDSS IV has been provided by the Alfred P. Sloan Foundation, the U.S. Department of Energy Office of Science, and the Participating Institutions. SDSS-IV acknowledges support and resources from the Center for High-Performance Computing at the University of Utah. The SDSS web site is www.sdss.org.

SDSS-IV is managed by the Astrophysical Research Consortium for the Participating Institutions of the SDSS Collaboration including the Brazilian Participation Group, the Carnegie Institution for Science, Carnegie Mellon University, the Chilean Participation Group, the French Participation Group, Harvard-Smithsonian Center for Astrophysics, Instituto de Astrofísica de Canarias, The Johns Hopkins University, Kavli Institute for the Physics and Mathematics of the Universe (IPMU) / University of Tokyo, the Korean Participation Group, Lawrence Berkeley National Laboratory, Leibniz Institut für Astrophysik Potsdam (AIP), Max-Planck-Institut für Astronomie (MPIA Heidelberg), Max-Planck-Institut für Astrophysik (MPA Garching), Max-Planck-Institut für Extraterrestrische Physik (MPE), National Astronomical Observatories of China, New Mexico State University, New York University, University of Notre Dame, Observatário Nacional / MCTI, The Ohio State University, Pennsylvania State University, Shanghai Astronomical Observatory, United Kingdom Participation Group, Universidad Nacional Autónoma de México, University of Arizona, University of Colourado Boulder, University of Oxford, University of Portsmouth, University of Utah, University of Virginia, University of Washington, University of Wisconsin, Vanderbilt University, and Yale University.

In addition, this research relied on resources provided to the eBOSS Collaboration by the National Energy Research Scientific Computing Center (NERSC). NERSC is a U.S. Department of Energy Office of Science User Facility operated under Contract No. DE-AC02-05CH11231.

The CosmoSim data base used in this paper is a service by the Leibniz-Institute for Astrophysics Potsdam (AIP). The MultiDark data base was developed in cooperation with the Spanish MultiDark Consolider Project CSD2009-00064.

The authors gratefully acknowledge the Gauss Centre for Supercomputing e.V. (www.gauss-centre.eu) and the Partnership for Advanced Supercomputing in Europe (PRACE, http://www.prace-ri.eu) for funding the MultiDark simulation project by providing computing time on the GCS Supercomputer SuperMUC at Leibniz Supercomputing Centre (LRZ, http://www.lrz.de).

DATA AVAILABILITY

All of the observational data sets used in this paper are available through the SDSS website https://data.sdss.org/sas/dr16/eboss/. The codes used in this analysis along with instructions are available on https://www.roe.ac.uk/~salam/MTHOD/. The outer rim halo catalogues are available on https://cosmology.alcf.anl.gov/.

REFERENCES

Alam S., Ho S., Silvestri A., 2016, MNRAS, 456, 3743
Alam S., Peacock J. A., Farrow D. J., Loveday J., Hopkins A. M., 2020, MNRAS, 503, 59
Alam S., Peacock J. A., Kraljic K., Ross A. J., Comparat J., 2019, MNRAS, 497, 581
Alam S., Zhu H., Croft R. A. C., Ho S., Giusarma E., Schneider D. P., 2017a, MNRAS, 470, 2822
Alam S. et al., 2017b, MNRAS, 470, 2617
Alam S. et al., 2020, Phys. Rev. D, 103, 083533
Avila S. et al., 2020, MNRAS, 499, 5486
Bautista J. et al., 2020, MNRAS, 500, 736
Behroozi P. S., Wechsler R. H., Wu H.-Y., 2013, ApJ, 762, 109
Bennett C. L. et al., 2013, ApJS, 208, 20
Benson A. J., Cole S., Frenk C. S., Baugh C. M., Lacey C. G., 2000, MNRAS, 311, 793
Berlind A. A., Weinberg D. H., 2002, ApJ, 575, 587
Beutler F. et al., 2012, MNRAS, 423, 3430
Beutler F. et al., 2017, MNRAS, 466, 2242
Bianchi D., Percival W. J., 2017, MNRAS, 472, 1106
Blake C. et al., 2011, MNRAS, 418, 1707
Blanton M. R. et al., 2017, AJ, 154, 28
Blas D., Lesgourgues J., Tram T., 2011, J. Cosmol. Astropart. Phys., 2011, 034
Cappi A., 1995, A&A, 301, 6
Carlson J., Reid B., White M., 2013, MNRAS, 429, 1674
Chen Y.-C. et al., 2017, MNRAS, 466, 1880
Cochrane R. K., Best P. N., 2018, MNRAS, 480, 864
Comparat J. et al., 2013a, MNRAS, 428, 1498
Comparat J. et al., 2013b, MNRAS, 433, 1146
Comparat J. et al., 2015, A&A, 575, A40
Comparat J. et al., 2016, A&A, 592, A121
Contreras S., Baugh C. M., Norberg P., Padilla N., 2013, MNRAS, 432, 2717
Cooray A., Sheth R., 2002, Phys. Rep., 372, 1
Davé R., Anglés-Alcázar D., Narayanan D., Li Q., Rafieferantsoa M. H., Appleby S., 2019, MNRAS, 486, 2827
Davis M., Efstathiou G., Frenk C. S., White S. D. M., 1985, ApJ, 292, 371
Dawson K. S. et al., 2013, AJ, 145, 10
Dawson K. S. et al., 2016, AJ, 151, 44
de-Mattia A. et al., 2020, MNRAS
de Jong R. S. et al., 2014, in Ground-based and Airborne Instrumentation for Astronomy V. p. 91470M
de la Torre S. et al., 2013, A&A, 557, A54
de Mattia A., Ruhlmann-Kleider V., 2019, J. Cosmol. Astropart. Phys., 2019, 036
DESI Collaboration, 2016, preprint (arXiv:1611.00036)
Dey A. et al., 2019, AJ, 157, 168
Dubois Y. et al., 2014, MNRAS, 444, 1453
du Mas des Bourboux H. et al., 2020, ApJ, 901, 153
Favole G. et al., 2016, MNRAS, 461, 3421
Geach J. E., Sobral D., Hickox R. C., Wake D. A., Smail I., Best P. N., Baugh C. M., Stott J. P., 2012, MNRAS, 426, 679
Gil-Marin H. et al., 2020, MNRAS, 498, 2492
Gonzalez-Perez V., Lacey C. G., Baugh C. M., Lagos C. D. P., Helly J., Campbell D. J. R., Mitchell P. D., 2014, MNRAS, 439, 264
Gonzalez-Perez V. et al., 2018, MNRAS, 474, 4024

Gonzalez-Perez V. et al., 2020, MNRAS, 498, 1852
Grieb J. N., Sánchez A. G., Salazar-Albornoz S., Dalla Vecchia C., 2016, MNRAS, 457, 1577
Gunn J. E. et al., 2006, AJ, 131, 2332
Guo H. et al., 2018, ApJ, 871, 147
Guo Q. et al., 2011, MNRAS, 413, 101
Habib S. et al., 2016, New Astron., 42, 49
Hamilton A. J. S., 1992, ApJ, 385, L5
Hand N., Feng Y., Beutler F., Li Y., Modi C., Seljak U., Slepian Z., 2018, AJ, 156, 160
Heitmann K. et al., 2019, ApJS, 245, 16
Hou J. et al., 2020, MNRAS, 500, 1201
James F., Roos M., 1975, Comput. Phys. Commun., 10, 343
Kaiser N., 1987, MNRAS, 227, 1
Klypin A., Yepes G., Gottlöber S., Prada F., Heß S., 2016, MNRAS, 457, 4340
Komatsu E. et al., 2011, ApJS, 192, 18
Kraljic K. et al., 2018, MNRAS, 474, 547
Kraljic K. et al., 2020, MNRAS, 491, 4294
Kravtsov A. V., Berlind A. A., Wechsler R. H., Klypin A. A., Gottlöber S., Allgood B. o., Primack J. R., 2004, ApJ, 609, 35
Laureijs R. et al., 2011, preprint (arXiv:1110.3193)
Lin S. et al., 2020, MNRAS, 498, 5251
Liske J. et al., 2015, MNRAS, 452, 2087
Lyke B. W. et al., 2020, ApJs, 250, 8
Matsubara T., 2008a, Phys. Rev. D, 77, 063530
Matsubara T., 2008b, Phys. Rev. D, 78, 083519
Matsubara T., 2008c, Phys. Rev. D, 78, 109901
McCarthy I. G., Schaye J., Bird S., Le Brun A. M. C., 2017, MNRAS, 465, 2936
McDonald P., Roy A., 2009, J. Cosmol. Astropart. Phys., 2009, 020
Mo H., van den Bosch F. C., White S., 2010, Galaxy Formation and Evolution. Cambridge University Press
Mohammad F. G. et al., 2020, MNRAS, 498, 128
Mostek N., Coil A. L., Cooper M., Davis M., Newman J. A., Weiner B. J., 2013, ApJ, 767, 89
Mueller E.-M., Percival W., Linder E., Alam S., Zhao G.-B., Sánchez A. G., Beutler F., Brinkmann J., 2018, MNRAS, 475, 2122
Myers A. D. et al., 2015, ApJS, 221, 27
Neveux R. et al., 2020, MNRAS, 499, 210
Newman J. A. et al., 2013, ApJS, 208, 5
Okumura T., Seljak U., Vlah Z., Desjacques V., 2014, J. Cosmol. Astropart. Phys., 2014, 003
Orsi Á. A., Angulo R. E., 2018, MNRAS, 475, 2530
Palanque-Delabrouille N. et al., 2016, A&A, 587, A41
Peacock J. A., Smith R. E., 2000, MNRAS, 318, 1144
Peebles P. J. E., 1980, The Large-Scale Structure of The Universe. Princeton University press
Percival W. J. et al., 2004, MNRAS, 353, 1201
Pillepich A. et al., 2018, MNRAS, 473, 4077
Planck Collaboration VI, 2018, A&A , 641, A6
Prada F., Klypin A. A., Cuesta A. J., Betancort-Rijo J. E., Primack J., 2012, MNRAS, 423, 3018
Prakash A. et al., 2016, ApJS, 224, 34
Raichoor A. et al., 2016, A&A, 585, A50
Raichoor A. et al., 2017, MNRAS, 471, 3955
Raichoor A. et al., 2020, MNRAS, 500, 3254
Reid B. A., Seo H.-J., Leauthaud A., Tinker J. L., White M., 2014, MNRAS, 444, 476
Reid B. A., White M., 2011, MNRAS, 417, 1913
Renneby M., Henriques B. M. B., Hilbert S., Nelson D., Vogelsberger M., Angulo R. E., Springel V., Hernquist L., 2020, MNRAS, 498, 5804
Riebe K. et al., 2013, Astron. Nachr., 334, 691
Ross A. et al., 2020, MNRAS, 498, 2354
Rossi G. et al., 2020, MNRAS
Schaye J. et al., 2010, MNRAS, 402, 1536
Schaye J. et al., 2015, MNRAS, 446, 521
Schlegel D., White M., Eisenstein D., 2009, in Astro2010: The Astronomy and Astrophysics Decadal Survey. p. 314, preprint (arXiv:0902.4680)
Seljak U., 2000, MNRAS, 318, 203
Smee S. A. et al., 2013, AJ, 146, 32
Smith A. et al., 2020, MNRAS, 499, 269
Spergel D. et al., 2015, preprint (arXiv:1503.03757)
Takada M. et al., 2014a, PASJ, 66, R1
Takada M. et al., 2014b, PASJ, 66, R1
Tamone A. et al., 2020, MNRAS, 499, 5527
Taruya A., Nishimichi T., Saito S., 2010, Phys. Rev. D, 82, 063522
Tasitsiomi A., Kravtsov A. V., Wechsler R. H., Primack J. R., 2004, ApJ, 614, 533
Vale A., Ostriker J. P., 2004, MNRAS, 353, 189
van Daalen M. P., McCarthy I. G., Schaye J., 2020, MNRAS, 491, 2424
Vlah Z., Castorina E., White M., 2016, J. Cosmol. Astropart. Phys., 2016, 007
Wang L., Reid B., White M., 2014, MNRAS, 437, 588
Wechsler R. H., Tinker J. L., 2018, ARA&A, 56, 435
White M., 2014, MNRAS, 439, 3630
White M., Hernquist L., Springel V., 2001, ApJ, 550, L129
White M. et al., 2011, ApJ, 728, 126
Wilson M. J., Peacock J. A., Taylor A. N., de la Torre S., 2017, MNRAS, 464, 3121
Zentner A. R., Hearin A., van den Bosch F. C., Lange J. U., Villarreal A., 2019, MNRAS, 485, 1196
Zhao C. et al., 2021, MNRAS, 503, 1149
Zheng Z. et al., 2005, ApJ, 633, 791
Zhu H., Alam S., Croft R. A. C., Ho S., Giusarma E., 2017, MNRAS, 471, 2345

[1]*Institute for Astronomy, University of Edinburgh, Royal Observatory, Blackford Hill, Edinburgh EH9 3HJ, UK*
[2]*IRFU, CEA, Université Paris-Saclay, F-91191 Gif-sur-Yvette, France*
[3]*Institute of Physics, Laboratory of Astrophysics, Ecole Polytechnique Fédérale de Lausanne (EPFL), Observatoire de Sauverny, CH-1290 Versoix, Switzerland*
[4]*Departamento de Física Teórica, Facultad de Ciencias, Universidad Autónoma de Madrid, E-28049 Cantoblanco, Madrid, Spain*
[5]*Instituto de Fsica Teorica, UAM-CSIC, Universidad Autonoma de Madrid, E-28049 Cantoblanco, Madrid, Spain*
[6]*Institute of Cosmology and Gravitation, Portsmouth University, Burnaby Road, Portsmouth PO13FX, UK*
[7]*Astrophysics Research Institute, Liverpool John Moores University, 146 Brownlow Hill, Liverpool L3 5RF, UK*
[8]*IRFU, CEA, Université Paris-Saclay, F-91191 Gif-sur-Yvette, France*
[9]*Center for Cosmology and AstroParticle Physics, The Ohio State University, Columbus, OH 43210, USA*
[10]*Institute of Cosmology & Gravitation, Dennis Sciama Building, University of Portsmouth, Portsmouth PO1 3FX, UK*
[11]*Max-Planck-Institut für extraterrestrische Physik (MPE), Giessenbachstrasse 1, D-85748 Garching bei München, Germany*
[12]*Department of Physics and Astronomy, University of Utah, Salt Lake City, UT 84112, USA*
[13]*Aix Marseille Univ, CNRS/IN2P3, CPPM, 13009 Marseille, France*
[14]*Institut de Ciències del Cosmos, Universitat de Barcelona, ICCUB, Martí i Franquès 1, E-08028 Barcelona, Spain*
[15]*Institut d'Estudis Espacials de Catalunya (IEEC), E-08034 Barcelona, Spain*
[16]*High Energy Physics Division, Argonne National Laboratory, Lemont, IL 60439, USA*
[17]*Computational Science Division, Argonne National Laboratory, Lemont, IL 60439, USA*
[18]*Max-Planck-Institut für Extraterrestrische Physik, Postfach 1312, Giessenbachstr, D-85748 Garching bei München, Germany*
[19]*Waterloo Centre for Astrophysics, University of Waterloo, Waterloo, ON N2L 3G1, Canada*

[20]*Department of Physics and Astronomy, University of Waterloo, Waterloo, ON N2L 3G1, Canada*
[21]*Sub-department of Astrophysics, Department of Physics, University of Oxford, Denys Wilkinson Building, Keble Road, Oxford OX1 3RH, UK*
[22]*Aix Marseille Univ, CNRS, CNES, LAM, 13013 Marseille, France*
[23]*Perimeter Institute for Theoretical Physics, 31 Caroline St North, Waterloo, ON N2L 2Y5, Canada*
[24]*Department of Physics and Astronomy, Sejong University, Seoul 143-747, Korea*
[25]*School of Physics and Astronomy, University of St Andrews, St Andrews KY16 9SS, UK*
[26]*Instituto de Física, Universidad Nacional Autónoma de México, Apdo. Postal 20-364, Ciudad de México, México*
[27]*National Astronomy Observatories, Chinese Academy of Science, Beijing 100012, P. R. China*
[28]*College of Astronomy and Space Sciences, University of Chinese Academy of Sciences, Beijing 100049, China*

This paper has been typeset from a TEX/LATEX file prepared by the author.